Rhombicuboctahedron unit cell based scaffolds for bone regeneration: geometry optimization with a mechanobiology – driven algorithm

Rhombicuboctahedron Unit Cell Based Scaffolds for Bone Regeneration: Geometry Optimization with a Mechanobiology – driven Algorithm

Antonio Boccaccio*, Michele Fiorentino, Antonio E. Uva, Luca N. Laghetti, Giuseppe Monno

Dipartimento di Meccanica, Matematica e Management, Politecnico di Bari, Bari 70126, Italy

*Corresponding author:

Dr. Antonio Boccaccio

Mailing Address:

Dipartimento di Meccanica, Matematica e Management

Politecnico di Bari

Viale Japigia, 182

70126, Bari

Italy

Contact Information:

Tel: +39-0805962705

Fax: +39-0805962777

E-mail: a.boccaccio@poliba.it

ABSTRACT

In a context more and more oriented towards customized medical solutions, we propose a mechanobiology-driven algorithm to determine the optimal geometry of scaffolds for bone regeneration that is the most suited to specific boundary and loading conditions. In spite of the huge number of articles investigating different unit cells for porous biomaterials, no studies are reported in the literature that optimize the geometric parameters of such unit cells based on mechanobiological criteria. Parametric finite element models of scaffolds with rhombicuboctahedron unit cell were developed and incorporated into an optimization algorithm that combines them with a computational mechanobiological model. The algorithm perturbs iteratively the geometry of the unit cell until the best scaffold geometry is identified, i.e. the geometry that allows to maximize the formation of bone. Performances of scaffolds with rhombicuboctahedron unit cell were compared with those of other scaffolds with hexahedron unit cells. We found that scaffolds with rhombicuboctahedron unit cell are particularly suited for supporting medium-low loads, while, for higher loads, scaffolds with hexahedron unit cells are preferable. The proposed algorithm can guide the orthopaedic/surgeon in the choice of the best scaffold to be implanted in a patient-specific anatomic region.

Keywords: Computational Mechanobiology; Morphology Optimization; Scaffold Unit Cell; Rhombicuboctahedron.

1. Introduction

Design of scaffolds for bone tissue engineering is a very challenging task that requires multi-disciplinary and multi-scale approaches [1,2]. Recent researches demonstrated that geometry and elastic properties of porous scaffolds significantly influence the cellular response and the rate of bone tissue regeneration process [3,4]. However, to date, a deep knowledge of the complex biological and biophysical phenomena that take place during the bone regeneration and that clearly explains how the scaffold geometry affects this process, is missing. The identification of all the geometrical features that might have an influence on bone tissue regeneration requires the systematic study of different classes of pore shapes but no such studies are currently available in the literature [3]. Very often, in order to partially bridge this information gap, scaffold designers utilize computational mechanobiological models that, combined with *in vivo* and *in vitro* experiments allow to gain a deeper understanding of the possible relationships existing between the cellular process of mechano-transduction, the mechanical environment and the scaffold geometry [5-11]. In other words, computational mechanobiological models are often utilized to determine the quantitative rules that govern the effects of mechanical and geometrical factors on tissue differentiation and bone regeneration in bone tissue scaffolds [12]. A number of recent papers using multi-physics modelling have investigated the effects of biophysical stimuli on bone cells in scaffolds. Jungreuthmayer *et al.* [13] quantified the deformation of cells seeded on a collagen-GAG scaffold which was perfused by culture medium inside a flow perfusion bioreactor. McCoy *et al.*, [14] examined how the scaffold mean pore size influences cell attachment morphology and subsequently impacts upon cell deformation and detachment when subjected to fluid-flow. Zhao *et al.* [15] determined the mechanical stimulation of osteoblasts seeded in a biomaterial scaffold under flow perfusion and mechanical compression using multiscale modelling by twoway fluid–structure interaction and FE approaches. Zhao *et al.* [16] applied a fluid–structure interaction model to investigate the role of scaffold geometry

(architecture, pore size and porosity) on pore wall shear stress under a range of different loading scenarios. Other authors predicted and measured in vivo stress and strain stimuli [17-21].

Following the recent development of more and more sophisticated rapid prototyping techniques that allow the fabrication of solids with arbitrarily complex geometry, an increasing attention was devoted to the design of unit cell geometries for regular porous biomaterials [22]. Relationships between scaffold micro-architecture and resulting mechanical and biological properties were extensively investigated in a number of articles [23-30]. Different unit cell geometries were studied such as cubic, rhombic dodecahedron, pyramidal and diamond and for some of them an analytical solution was derived that expresses the apparent mechanical properties in function of the unit cell geometric parameters. For instance, based on the Euler-Bernoulli beam theory, Hedayati *et al.* developed the analytical solutions that relate the dimensions of the repeating unit cell to the elastic modulus, Poisson's ratio and yield stress of porous biomaterials based on the rhombicuboctahedron [31] and the truncated cube [32] unit cells. Despite these studies, our understanding of mechanobiology of tissue differentiation in scaffolds remains still incomplete and to the knowledge of the present authors, no studies are reported in the literature that optimize the geometric parameters of such unit cells based on mechanobiological criteria. The optimization of the geometry of bone tissue scaffolds is the objective of a number of studies [33]. Most of them identified the best scaffold geometry based on criteria other than the mechanobiological ones [34-38]. In previous studies, we developed a mechanobiology-based optimization algorithm to determine the best scaffold geometry with both, constant [39] and functionally graded [40] porosity. The scaffolds investigated in these studies included a simple hexahedron unit cell obtained as a cubic volume with three holes generated, each, as the cut-protusion of rectangular (or, in the simpler case, square) or elliptic (or, in the simpler case, circular) contours along the three orthogonal directions of the coordinate axes. In the present study, we further developed this model by including a much more complex and sophisticated unit cell, i.e. the rhombicuboctahedron unit cell. The recent interest devoted to this relatively unexplored unit cell [31] led us to investigate its mechanobiological behaviour as well as to compare its

performances with those of hexahedron unit cell. The beam elements of which the rhombicuboctahedron unit cell is comprised were hypothesized to possess both, square and circular cross-section. In detail, the proposed algorithm combines a computational mechanobiological model, a structural optimization routine and the Finite Element (FE) model of a scaffold subjected to compression load. The algorithm perturbs iteratively the geometry of the unit cell and hence of the entire scaffold model until the best scaffold geometry is identified, i.e. the geometry that allows maximizing the amounts of bone predicted to form. The optimal scaffold geometry was determined for different levels of the: (i) scaffold Young's modulus, (ii) load acting on the scaffold and (iii) length of each beam element included in the unit cell.

2. Materials and Methods

2.1. CAD models of the rhombicuboctahedron unit cell and of the entire scaffold

The model of the unit cell successively discretized into finite elements, was first generated in CAD environment. Both, the CAD and finite element models were generated through the general purpose software ABAQUS® Version 6.12 (Dassault Systèmes, France). In detail, the generation of CAD was performed by adopting a seven-step procedure. In the first step (Fig. 1(a)), an octagonal trajectory t_{oct} was traced, a circular or square cross-section was created and then protruded, by means of the tool 'sweep' available in ABAQUS, along t_{oct}. All the sides of t_{oct} trajectory were hypothesized to have the same length L. The same procedure described for step 1 was successively repeated in steps 2 to 6, (Figs 1(b) to 1(f)) adding a solid volume - protruded along octagonal trajectories t_{oct} - in each step. In step 7 (Fig. 1(g)) the solid so obtained was cut along planes π_{Mi} (i=1, 2, …6) delimiting the cubic volume $Q \times Q \times Q$ containing the unit cell. Dimension Q is related to the length L of each side of t_{oct} through the relationship:

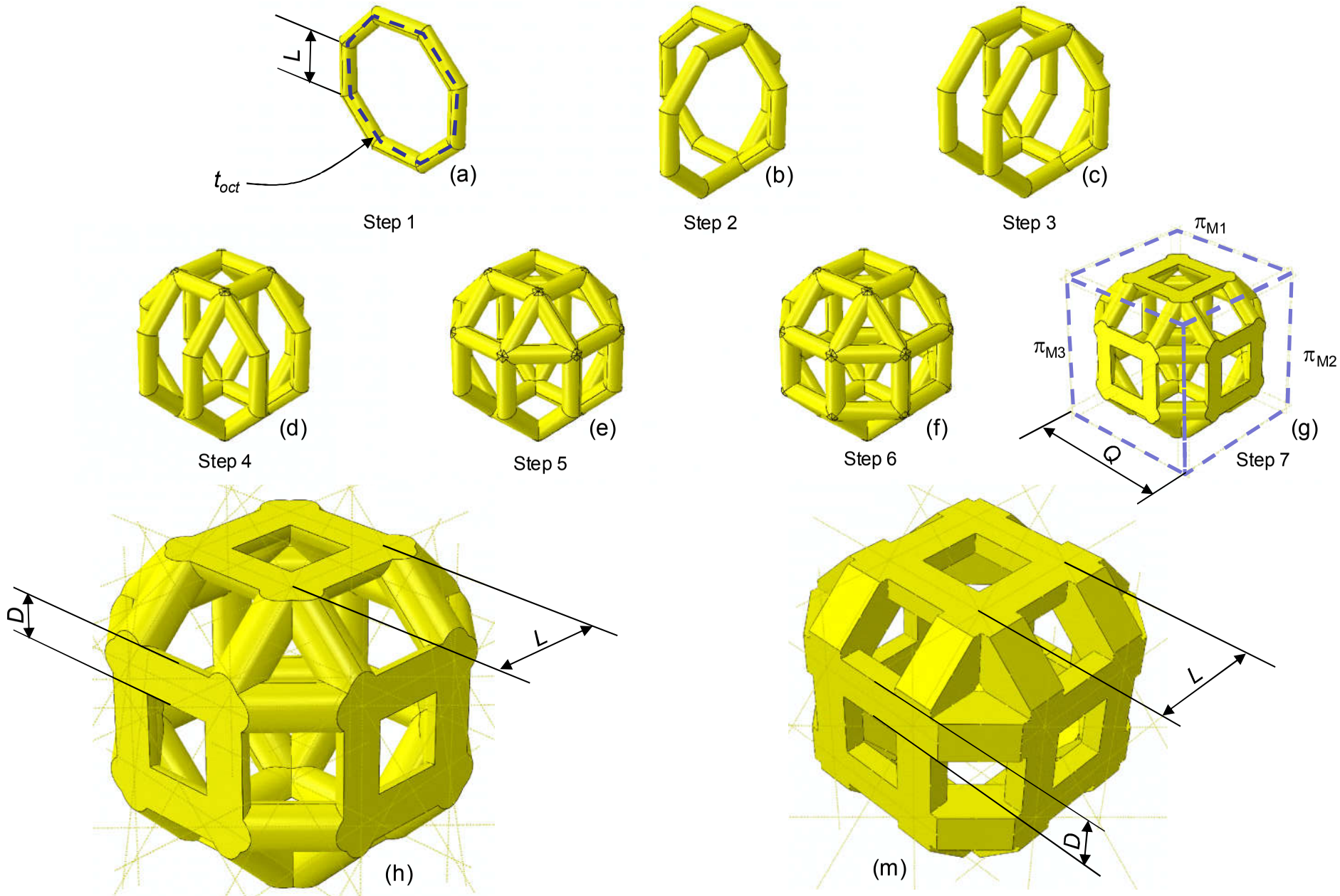

Fig. 1. The generation of the rhombicuboctahedron unit cell was performed in seven subsequent steps (a-g). In the first step (a), an octagonal trajectory t_{oct} was traced, a circular or square cross-section was created and then, through the tool 'sweep' available in ABAQUS, a solid with the fixed cross-section was protruded along t_{oct}. All the sides of the octagonal trajectory t_{oct} were hypothesized to be equal and long L. The same procedure described in the first step (a) was successively repeated in the steps 2 to 5 ((b) to (f)) by adding a solid volume (protruded along t_{oct}) in each step. In the step 7 (g) the solid so obtained was cut along planes π_{Mi} (i=1, 2, …6) delimiting the cubic volume ($Q \times Q \times Q$, $Q = L \times (1 + 2 \cos(\pi/4))$ containing the unit cell. Rhombicuboctahedron unit cells with circular (h) and square (m) cross-section investigated in the study with indicated the dimensions L and D parameterized in the study. Three different values of L were hypothesized: $L = L_0 = 263{,}85$ μm, $L = L_- = L_0 \times 0{,}9$ and $L = L_+ = L_0 \times 1{,}1$. The entire scaffold geometry was obtained by successively mirroring the unit cell with respect to π_{Mi} planes.

$$Q = L \cdot \left(1 + 2 \cdot \cos\left(\frac{\pi}{4}\right)\right) \quad (1)$$

Protrusions were carried out with a circular (Fig. 1(h)) or a square (Fig. 1(m)) cross-section. Three different values of L were hypothesized: $L = L_0 = 263.85$ μm, $L = L_- = L_0 \times 0.9$ and $L = L_+ = L_0 \times 1.1$. With these values, the resulting scaffold dimensions are consistent with those hypothesized in previous studies [39,40]. The cross-section dimension D, i.e. the diameter of the circular cross-section (Fig. 1(h)) and/or the side length of the square cross-section (Fig. 1(m)) was fixed as a parametric variable and its value was optimized via the algorithm described below.

By successively mirroring the unit cell with respect to planes π_{Mi} the entire scaffold geometry including $4 \times 4 \times 4 = 64$ unit cells was obtained (Fig. 2). According to previous studies [5] the volume enclosed within the scaffold structure, - i.e. the volume of the scaffold pores, - was hypothesized to be occupied by granulation tissue. The CAD model of this tissue (represented in red, Fig. 2(b)) was generated through the boolean operation of subtraction (from the cubic volume $4Q \times 4Q \times 4Q$, the volume occupied by the scaffold itself). The resulting scaffold system (scaffold + granulation tissue) had dimensions $h \times h \times h$ (Fig. 2(c)), where h is a function of L. In particular, in the case where $L = L_0$, it was $h = h_0 = 4 \times Q = 4 \times L_0 \times (1 + 2 \times \cos(\pi/4)) = 4 \times 637 = 2548$ μm; analogously, in the case $L = L_-$, it was $h = h_0 \times 0.9 = 2293.2$ μm; finally, in the case $L = L_+$, it was $h = 1.1 \times h_0 = 2802.8$ μm. Values of h investigated in this study are consistent with those hypothesized in previous articles [39,40].

Exploiting the symmetry of the system with respect to the planes $\pi_{1\text{-}2}$ and $\pi_{3\text{-}2}$ (Fig. 2(c)), only 1/4 of the entire model was studied that included $2 \times 2 \times 4 = 16$ unit cells for a total volume $V_{TOT} = h/2 \times h/2 \times h$ (Fig. 2(d)).

2.2. Finite element modelling of scaffolds subjected to compression loading

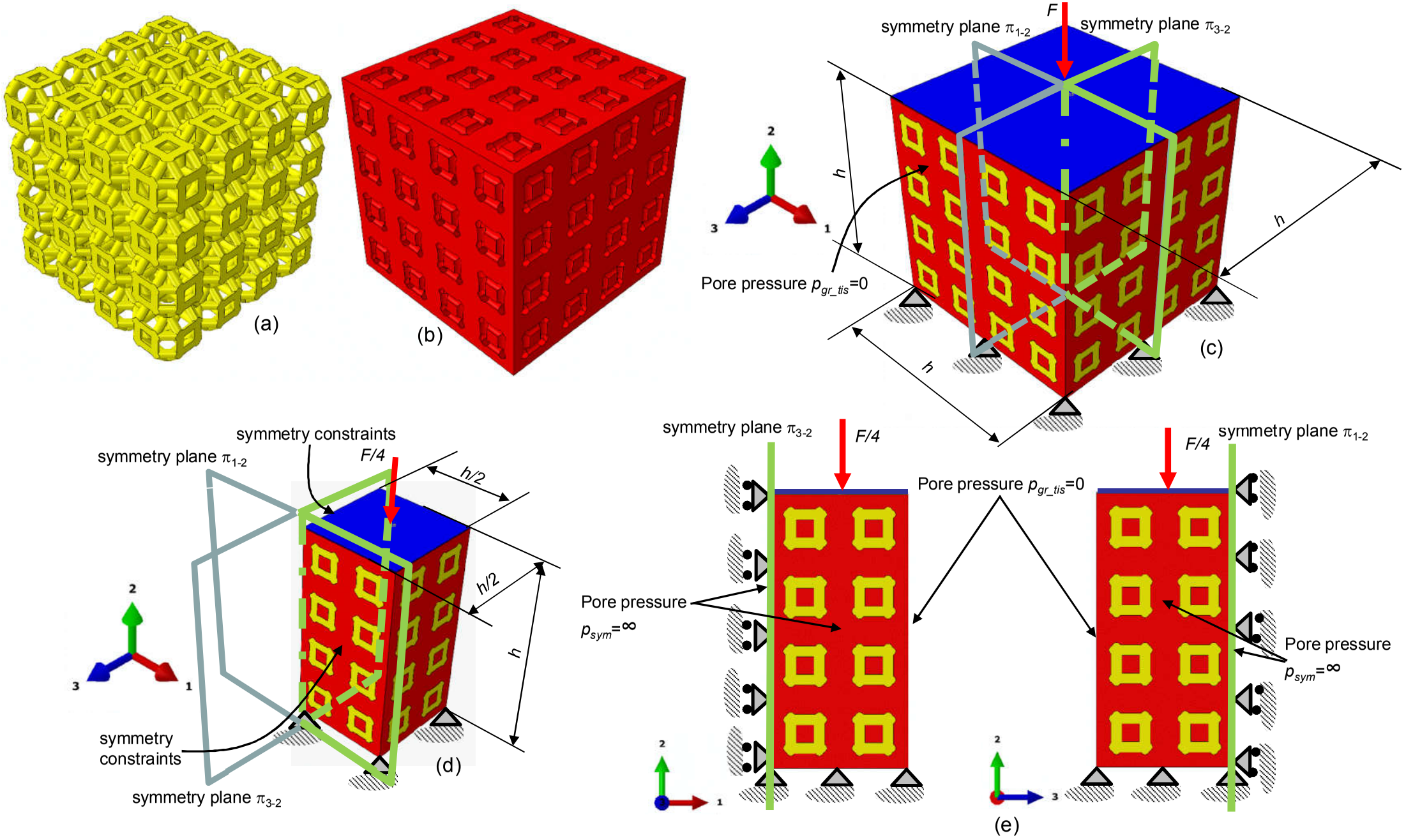

Fig. 2. Boundary and loading conditions acting on the scaffold model. CAD model of the scaffold (a), granulation tissue (b) and entire (including 64 unit cells) system (scaffold + granulation tissue) (c). Exploiting the symmetry of the problem, a simplified model reproducing only 1/4 of the entire geometry was considered (d). (e) Detailed views of the simplified model with indicated the boundary and loading conditions acting on it. As the surrounding tissue would not totally prevent the fluid from escaping, the pore pressure p_{gr_tis} on the outer surfaces of the granulation tissue was set equal to zero to simulate the free exudation of fluid. On the symmetry planes instead, being null the fluid flow, the pore pressure must be p_{sym}= ∞.

The CAD models with both, circular and square cross-sections were discretized into finite elements (Fig. 3). Models of scaffold and granulation tissue were hypothesized to be made from poroelastic materials and discretized with tetrahedral four-node, linear displacement and pore pressure elements (C3D4P, see ABAQUS Documentation). Setting an average element dimension of 20 μm, the model (i.e. scaffold + granulation tissue) included about 5×10^6 elements with about 1×10^6 nodes.

The scaffold model was hypothesized to be subjected to compression loading. To this purpose, the nodes of the bottom surface were clamped (Figs. 2(c) to 2(e)) while a compression load was applied on the scaffold upper surface via a rigid plate (represented in blue, Fig. 2). Constraint equations were utilized between the rigid plate (RP) and the scaffold upper surface (SUS) to impose the equality of the displacement fields u_2 of the two surfaces: u_2 (RP) = u_2 (SUS) (Fig. 2(c)). The concentrated force F acting on the plate produces a uniformly distributed load p given by: $p = F / (h \times h)$, being $h \times h$ the area of the plate surface. F was hypothesized to assume five different values corresponding to the pressures p: 0.05, 0.1, 0.5, 1.0 and 1.5 MPa which are consistent with the pressure values hypothesized by Byrne *et al.* [5]. The load, according to previous articles [39,41], was applied following a linear ramp in the time interval of 1 second that is the hypothetical time in which a scaffold can be loaded in physiological conditions. The hypothesized values of pressure correspond to medium-low values of load acting on the spongy bone, which shows an ultimate strength in compression of 10÷20 MPa depending on its apparent density [42]. According to Byrne *et al.* [5], the pore pressure p_{gr_tis} acting on the outer surface of the granulation tissue was imposed to be nil, (Figs. 2(c) and 2(e)) which means that during the compression the fluid can freely exudate. Symmetry constraints were applied on the surfaces of the model lying on the symmetry planes $\pi_{1\text{-}2}$ and $\pi_{3\text{-}2}$ (Figs. 2(d) and 2(e)). In particular, an infinite pore pressure ($p_{sym} = \infty$) was applied on these surfaces which indicates that fluid flow is not allowed.

Regarding the mechanical properties implemented in the FE model, we hypothesized three different values of the scaffold Young's modulus: 500, 1000 and 1500 MPa, which are consistent with those utilized by Byrne *et al.* [5]. The same material properties were also utilized in previous

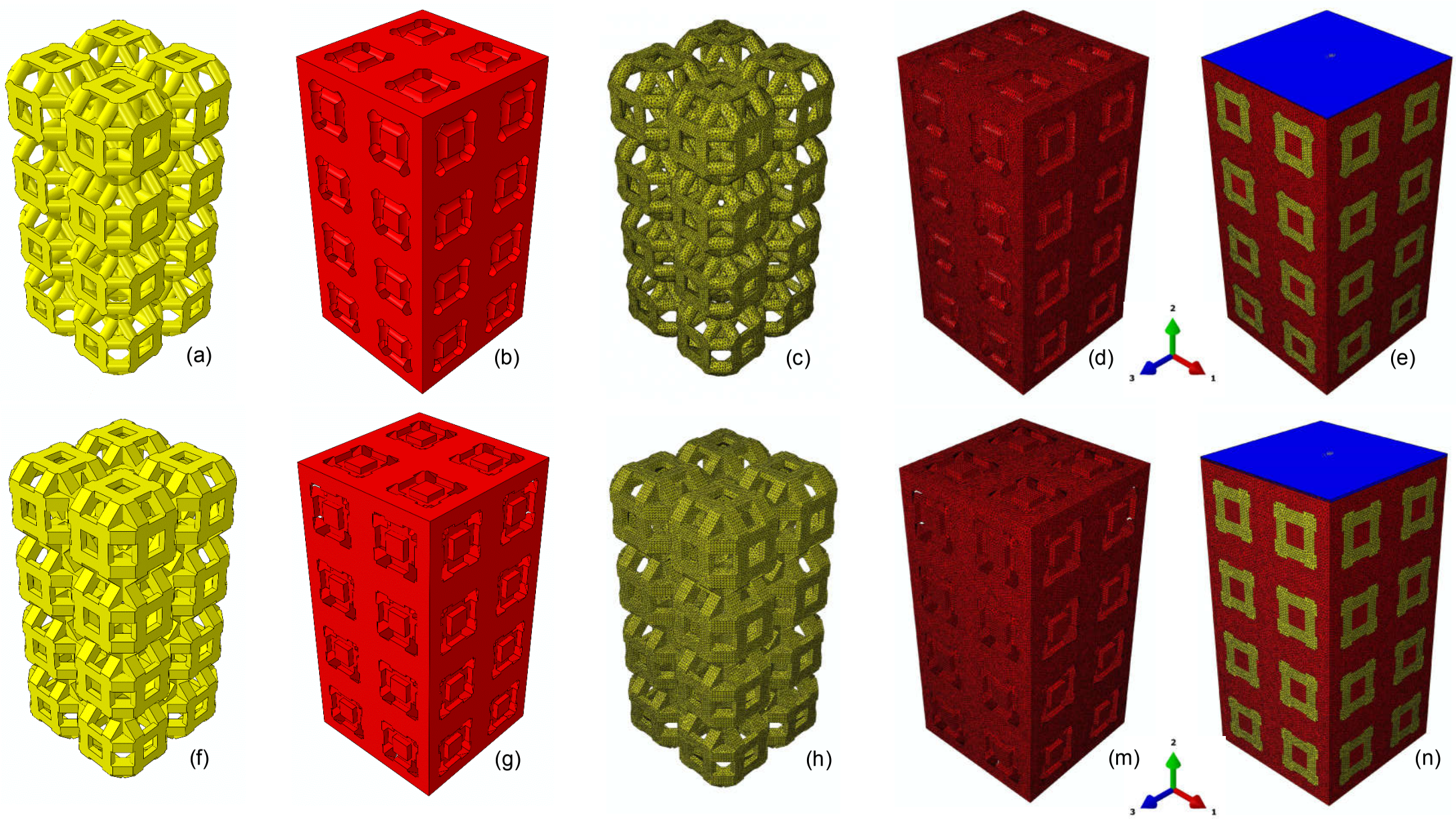

Fig. 3. CAD model of the scaffold (a, f) and of the granulation tissue (b, g) in the case of circular (a, b) and square (f, g) cross-section. Finite element mesh of the scaffold (c, h), the granulation tissue (d, m) and of the entire system (e, n) in the case of circular (c, d, e) and square (h, m, n) cross-section. The entire model (scaffold + granulation tissue) included about 5×10^6 elements with about 1×10^6 nodes.

studies [39,40]. An example of a real material used in fabricating scaffolds by selective laser sintering and possessing a Young's modulus reasonably close ($E \approx 500$ MPa) to those hypothesized in this study, is represented by the Polycaprolactone [43]. The other material properties implemented for the scaffold model are the following [5]: permeability, 1×10^{-14}m^4/N/s; porosity, 0.5; Poisson's ratio, 0.3; bulk modulus grain, 13920 MPa; bulk modulus fluid, 2300 MPa. Material properties implemented for the granulation tissue are the same as those utilized in other articles [44-46]: Young's modulus, 0.2 MPa; permeability 1×10^{-14}m^4/N/s; Poisson's ratio, 0.167; porosity, 0.8; bulk modulus grain, 2300 MPa; bulk modulus fluid, 2300 MPa.

Nonlinear finite element analyses were performed that account for geometric nonlinearities.

2.3. Mechanobiological model based on deviatoric strain and fluid velocity

Once the Mesenchymal Stem Cells (MSCs) invade the scaffold and occupy its pores, their differentiation begins thus triggering the tissue regeneration process. Following the hypothesis that the transient phase of the cells dispersal has already terminated we assume that MSCs are homogeneously distributed throughout the scaffold pores. Following the mechanobiological model of Prendergast *et al.* [47] and according to Byrne *et al.* [5], we modelled the domain where regeneration takes place as a poroelastic material and assumed the tissue differentiation process to depend on a biophysical stimulus S that is, in turn, a function of the octahedral shear strain γ and of the relative fluid/solid velocity v. In detail, if ε_I, ε_{II} and ε_{III} are the principal strains, and a and b the two empirical constants defined by Huiskes *et al.* [48] as $a = 3.75$ % and $b = 3$ μms^{-1}, the octahedral shear strain γ and the biophysical stimulus S are given by:

$$\begin{cases} \gamma = \frac{1}{2}\sqrt{(\varepsilon_I - \varepsilon_{II})^2 + (\varepsilon_{II} - \varepsilon_{III})^2 + (\varepsilon_I - \varepsilon_{III})^2} \\ S = \frac{\gamma}{a} + \frac{v}{b} \end{cases} \tag{2}$$

Based on the values of S, the model predicts formation of different tissue types. The following inequalities describe the tissue type corresponding to all the possible values S can assume:

$$\begin{cases} if\ S > c\ then\ fibrogenesis \rightarrow formation\ of\ fibrous\ tissue \\ if\ 1 < S < c\ then\ chondrogenesis \rightarrow formation\ of\ cartilage \\ if\ n_{mature} < S < 1\ then\ osteogenesis \rightarrow formation\ of\ immature\ bone \\ if\ n_{resorb} < S < n_{mature}\ then\ osteogenesis \rightarrow formation\ of\ mature\ bone \\ if\ 0 < S < n_{resorb}\ then\ osteoclastogenesis \rightarrow bone\ resorbtion \end{cases} \quad (3)$$

where n_{resorb}, n_{mature}, and m represent boundaries of the mechano-regulation diagram for tissue differentiation. Their values were taken to be the same as those utilized by Lacroix and Prendergast [49] (n_{resorb} = 0.01, n_{mature} = 0.53, m = 3). By utilizing the FE model above described, the strain and the fluid velocity values were computed within the volume of the scaffold pores (represented in red, Fig. 2(b)) and implemented into equations (2). Therefore, based on the values of S and according to inequalities (3) the tissue type for each element was predicted. The specific succession of all the operations followed to do this computation as well as the criterion utilized to determine the best scaffold geometry are described in the following section.

2.4. The optimization algorithm implemented to determine the best scaffold geometry

An *ad hoc* algorithm was written in Matlab® (Version R2015b) environment integrating: (a) CAD and FE scaffold models, (b) the mechano-regulation model described above and (c) a globally convergent gradient-based structural optimization routine. A graphical summary of this algorithm is shown in Fig. 4. The objective of the algorithm is to determine the best value of the cross-section dimension D (for different cross-section shapes and for different values of the: (i) scaffold Young's modulus E, (ii) length of the beam elements L and (iii) compressive load p) that allows to maximize the formation of bone. The algorithm first requires to select: (i) the shape (Block [1]) of the cross-section (circular or square, Block [2]); (ii) one of the three possible values (Block [3] and Block [4]) of the scaffold Young's modulus (i.e. E = 500, 1000 or 1500 MPa); (iii) one of the three possible

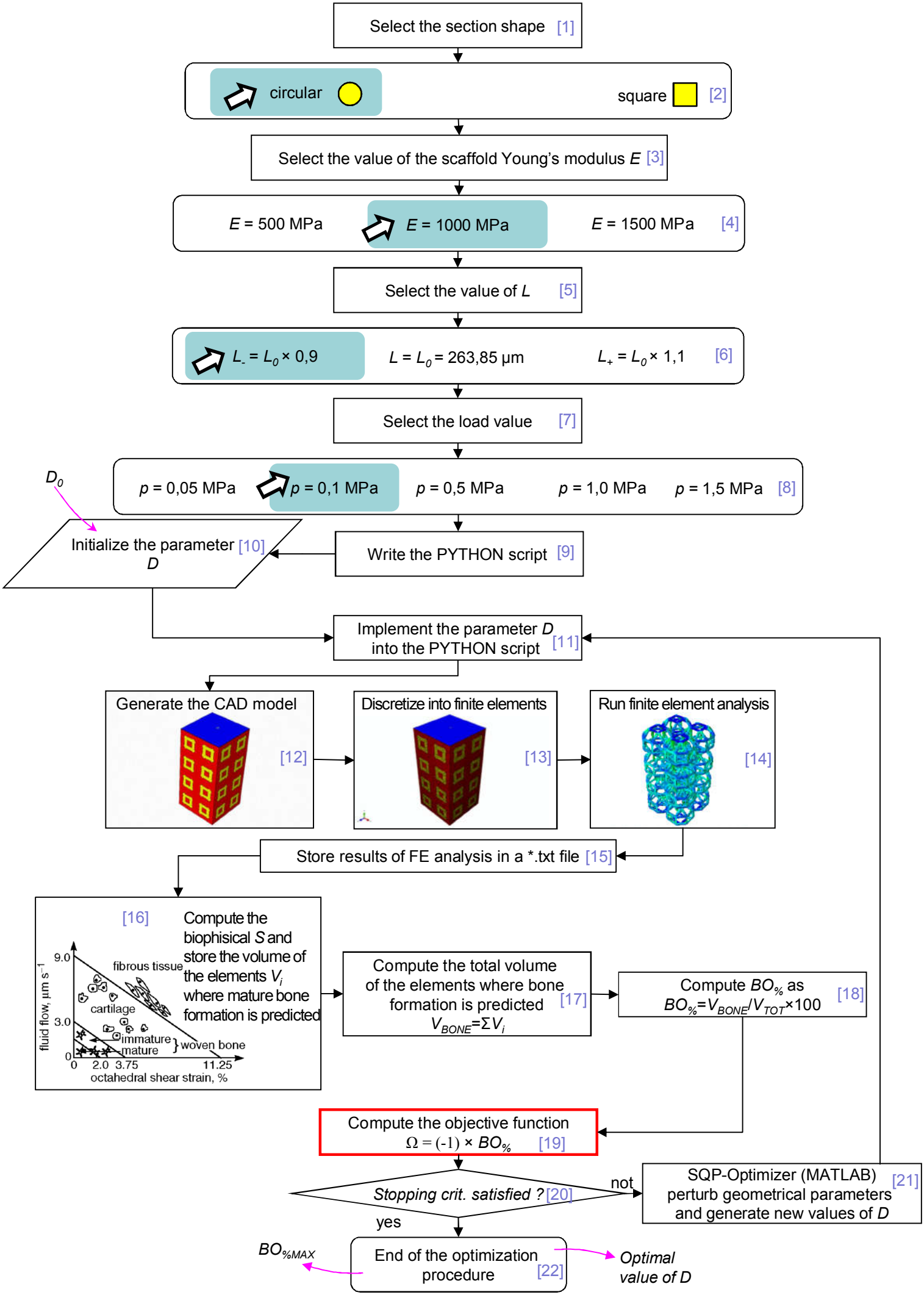

Fig. 4. Schematic of the algorithm written in Matlab environment to determine the optimal dimension D for different values of load, Young's modulus and L and for different cross-section shapes.

values of L (Block [5]) (Fig. 1, $L = L_0$, $L = L_-$ and $L = L_+$ (Block[6])); (iv) one of the five possible values of the load p (Block [7]) (p = 0.05, 0.1, 0.5, 1.0 and 1.5 MPa (Block [8])). Based on the choices made by the user, the algorithm writes the corresponding PYTHON script (Block [9]) and after asking the user to initialize the value of the cross-section dimension D (Block [10]) implements this value into the script itself (Block [11]). Then, the PYTHON script is given in input to ABAQUS that builds the CAD model (Block [12]), generates the finite element mesh (Block [13]) and runs the finite element analysis (Block [14]) with the boundary and loading conditions described above. Results of the FE analysis including the values of the principal strains and those of the relative fluid/solid velocity are stored in a *.txt file (Block [15]). According to equations (2) and (3), the algorithm computes, for all the elements occupying the scaffold pores (represented in red, Figs. 2 and 3), the biophysical stimulus S (Block [16]). In particular, for those elements where the formation of mature bone is predicted (i.e. for the elements for which the inequality $n_{resorb} < S < n_{mature}$ is satisfied) the algorithm stores the volume V_i. Once computation of S is terminated for all the elements, the algorithm calculates the volume V_{BONE} given by the sum of all the volumes V_i: $V_{BONE} = \Sigma V_i$, (Block [17]). Known V_{BONE}, $BO_{\%}$, the percentage of the total scaffold volume occupied by bone is computed as (Block [18]): $BO_{\%} = V_{BONE} / V_{TOT} \times 100$. At this point, the objective function Ω is defined as the opposite of $BO_{\%}$ (Block [19]) and an optimization problem is formulated, where the cross-section dimension D is the design variable while Ω is the objective to minimize:

$$\begin{cases} Min\ (\Omega\ (D) = (-1) \cdot BO_{\%}) \\ D_{min} < D < D_{max} \end{cases} \quad (4)$$

D_{min} and D_{max} are the lower and the upper bounds, respectively, that were hypothesized to assume the values listed in Fig. 5. In particular, regardless of the cross-section shape and of the value of L, D_{min} was set equal to 28 μm (Figs. 5 (a) and 5 (b)). For the hypothesized values of load, in fact, cross-section dimensions D smaller than 28 μm do not have any interest. Values of the upper bound D_{max},

L	Section shape	D_{min} [μm]	D_{max} [μm]
L_0	circular	28.0	154.0
L_-	circular	28.0	142.0
L_+	circular	28.0	168.0
L_0	square	28.0	109.0
L_-	square	28.0	98.0
L_+	square	28.0	120.0

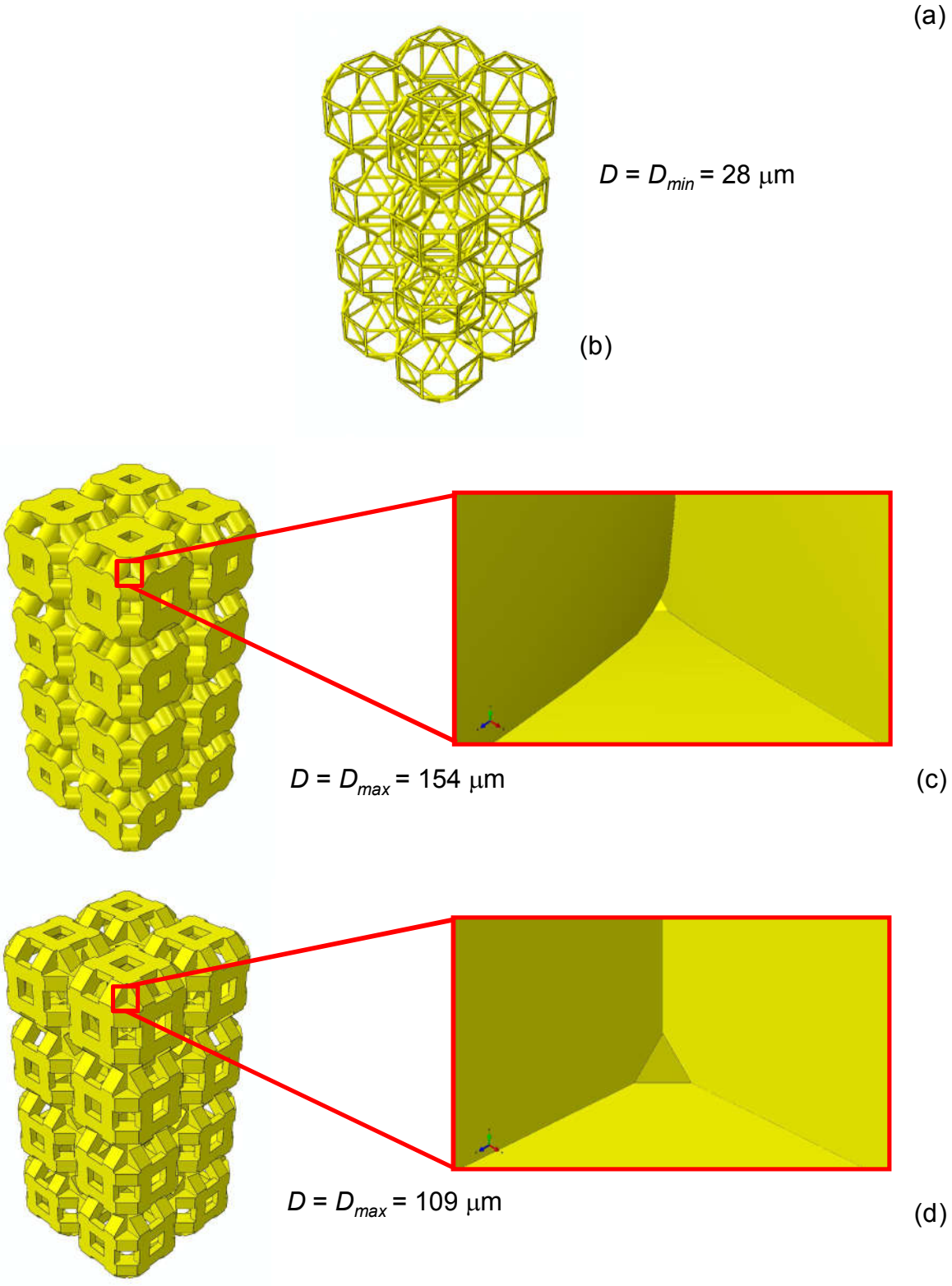

Fig. 5. (a) Upper and lower bounds set for the dimension D for different cross-section shapes and values of L. Geometric configuration of the model for $D = D_{min}$ (b) and $D = D_{max}$ in the case of circular (c) and square (d) cross-section. Values of $D > D_{max}$ lead to close the aperture between the inclined sides (see detailed images (c) and (d)) thus changing the originally hypothesized connectivity scaffold.

instead, were set in function of the cross-section shape and the beam length L. In general, values of $D > D_{max}$ lead to close the aperture between the inclined sides of the triangular elements of the unit cell (Figs. 5 (c) and 5 (d)) thus changing the originally hypothesized connectivity scaffold.

In order to solve the inverse problem described in equation (4), the optimization tool *fmincon* available in Matlab® was utilized, that finds the minimum of a constrained nonlinear multivariable function. The implementation of this solver requires the definition of stopping criteria that depend, in turn, on the tolerance values fixed by the user. If one of these stopping criteria is met (Block [20], Fig. 4), the algorithm stops and gives in output the optimal dimension of D and the corresponding value of the percentage of the total scaffold volume occupied by bone $BO_{\%MAX}$ (Block [22]). Conversely, if none of the stopping criteria is satisfied, the algorithm perturbs the scaffold geometry generating new candidate solutions D (Block [21]). These are implemented into the PYTHON script (Block [11]) that is given input to Abaqus thus commencing a new iteration cycle. It is worthy to note that for each iteration cycle, a value of $BO_{\%}$ is computed. Obviously, for how the objective function is defined, the value of $BO_{\%}$ computed in correspondence of the optimal dimension of D is the maximum one (among all the other $BO_{\%}$ computed in all the cycles performed) and is hence called $BO_{\%MAX}$ (see Fig. 4, Block [22]).

Each optimization process included, on average, thirty iteration cycles, which means, in other words, thirty finite element analyses to be run. Considering that each FE analysis took about 1.2 h, it follows that an entire optimization process required approximately $30 \times 1.5 = 36$ h. Furthermore, considering that in this study we investigated 2 cross-section shapes, three values of length L, three values of the scaffold Young's modulus and five levels of compressive loads, it follows that a total of: $2 \times 3 \times 5 \times 3 = 90$ optimization processes were carried out that took some 3200 h.

Computations were performed on a HP XW6600- Intel® Xeon® Dual-Processor E5-5450 3 GHz – 32 Gb RAM.

3. Results and Discussion

3.1. Effect of cross-section shape

The optimal scaffold geometries predicted by the algorithm in the case of circular (Fig. 6(a)) and square (Fig. 7(a)) cross-section were consistent with our expectations. The optimal cross-section dimension D increases for decreasing values of the scaffold Young's modulus E and for increasing levels of the compressive load p. In fact, as E decreases, the global scaffold stiffness decreases too, which implies higher strain values and hence larger formation of fibrous tissue. The algorithm, then, tends to counterbalance this, increasing the cross-section dimension thus stiffening the scaffold. In the same way, increasing values of p lead to larger deformations that lead, in turn, to higher levels of the biophysical stimulus S and hence to fibrogenesis (see equation 3). The algorithm tends 'to move' the average biophysical stimulus S towards the osteogenesis, by increasing D. Curves reporting the optimal dimension D in function of the load (per unit area) p monotonically increase until the asymptotic condition of saturation $D = D_{max}$ is reached (Figs. 6(b) and 6(c)). Once, for a load level, the condition $p = p_{saturation}$ is reached, then the algorithm gives in output, for all the values of $p > p_{saturation}$, the result $D = D_{max}$. As it can be seen (Figs. 6(b) and 7(b)), the saturation load $p_{saturation}$ depends on the scaffold Young's modulus and increases with it. Interestingly, $p_{saturation}$ values computed for the circular cross-section are on average higher than those predicted for the square one. In general, the higher the saturation load, the larger is the interval where the optimization algorithm can find the optimal solution and hence, definitively, the larger the amounts of bone that can create within the scaffold pores.

Increasing values of $BO_{\%MAX}$ are predicted for decreasing values of loads and for increasing scaffold Young's moduli, in both cases, circular (Fig. 6(c)) and square (Fig. 7(c)) cross-section.

If V_{SCAFF} is the volume occupied by the scaffold, the percentage of volume occupied by the scaffold is defined as $SCA_{\%} = V_{SCAFF}/V_{TOT} \times 100$. Similarly, the percentage of volume occupied by

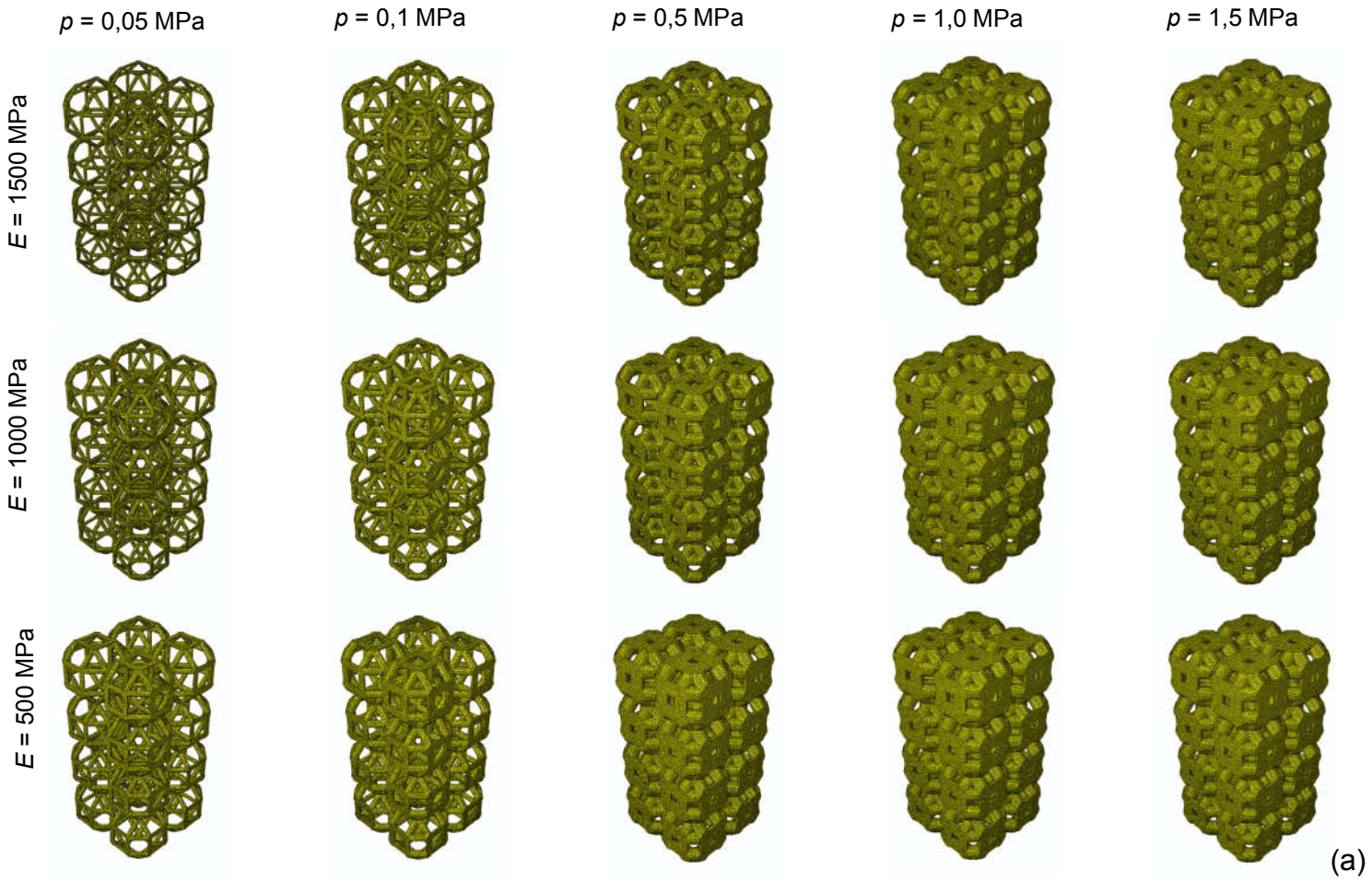

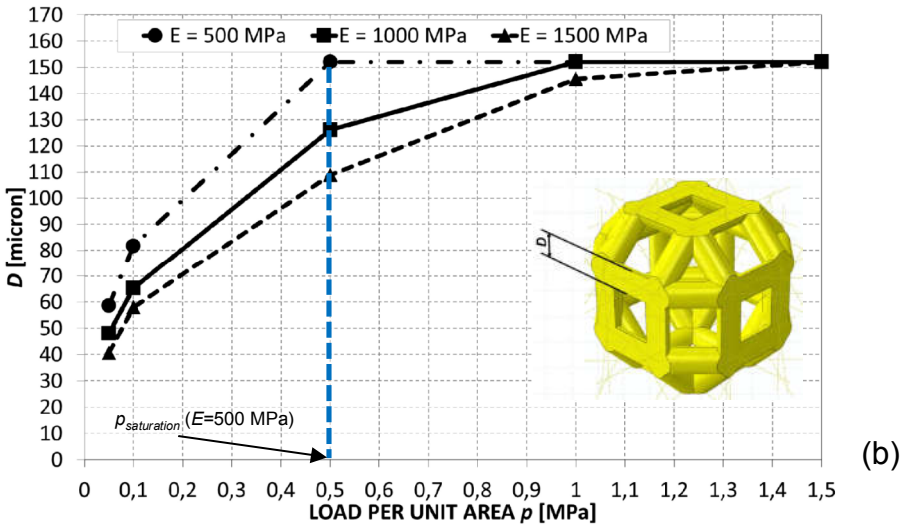

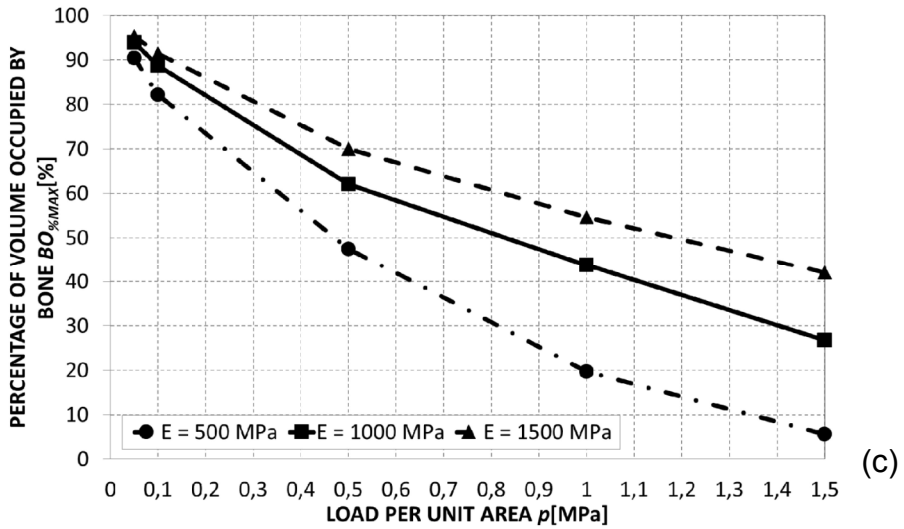

Fig. 6. Optimization of the rhombicuboctahedron unit cell, circular cross-section. (a) Optimal scaffold geometries predicted by the algorithm, in the case of circular cross-section. Values of the optimal diameter D (b) and of $BO_{\%MAX}$ (c) predicted by the algorithm for different levels of load and scaffold Young's modulus. For the sake of clarity, the only saturation load $p_{saturation}$ related to E = 500 MPa is shown in the figure.

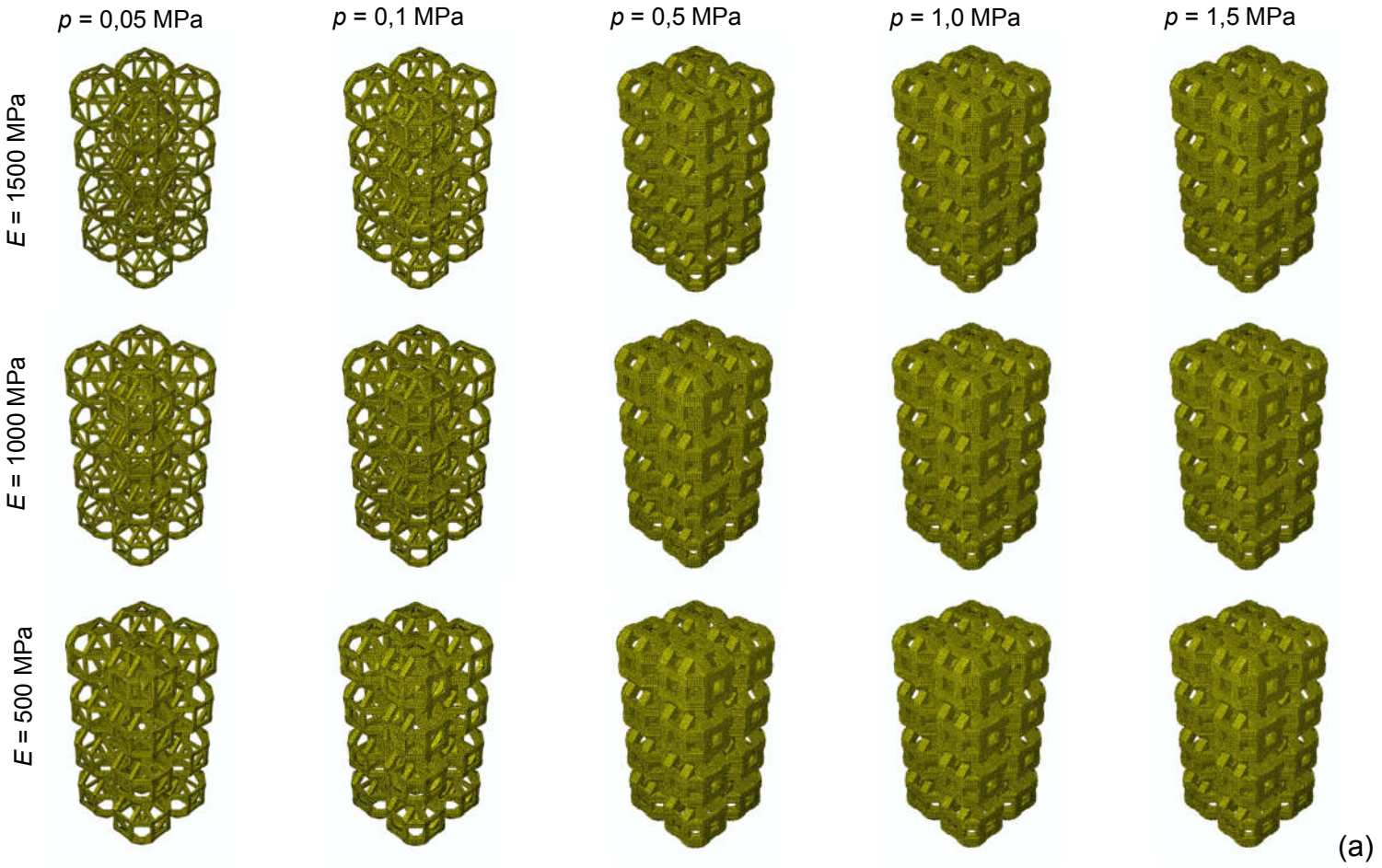

(a)

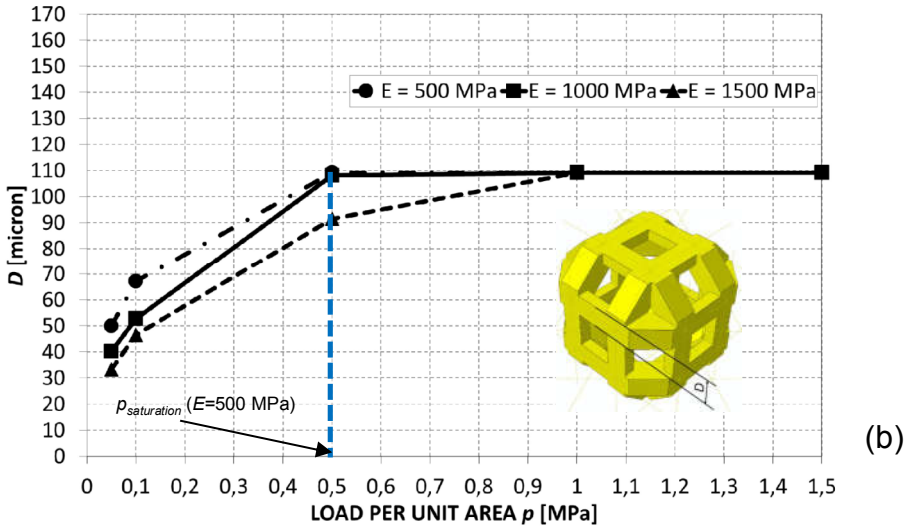

(b)

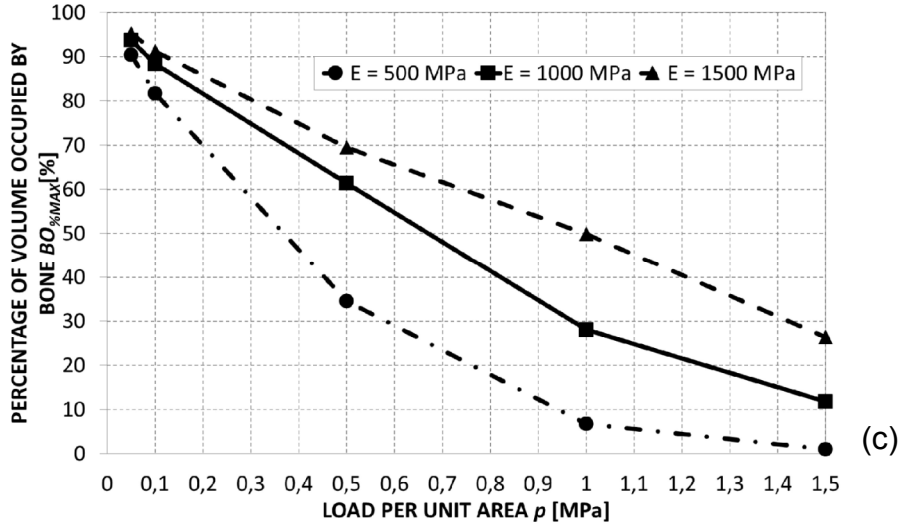

(c)

Fig. 7. Optimization of the rhombicuboctahedron unit cell, square cross-section. (a) Optimal scaffold geometries predicted by the algorithm, in the case of square cross-section. Values of the optimal diameter D (b) and of $BO_{\%MAX}$ (c) predicted by the algorithm for different levels of load and scaffold Young's modulus. For the sake of clarity, the only saturation load $p_{saturation}$ related to E = 500 MPa is shown in the figure.

Tissues Other than Mature Bone (TOMB) is defined as $TOMB_{\%} = (V_{TOT}-V_{SCAFF}-V_{BONE})/V_{TOT} \times 100$. Increasing amounts of TOMB are predicted for increasing levels of the load (Fig. 8). However, for all the hypothesized values of pressure, $TOMB_{\%}$ computed for the square cross-section (Fig. 8(b)) is larger than the circular cross-section counterpart (Fig. 8(a)). The percentage of volume occupied by scaffold $SCA_{\%}$ in the case of the circular (Fig. 8(a)) cross-section, instead, appears to be larger than that predicted for the square cross-section (Fig. 8(b)) especially in the case of high load levels. In a not optimized configuration (for example, in Fig. 8(c), the optimized (D = 58 μm, Fig. 6(b)) and not optimized (D = 40 μm) configuration of a scaffold with circular section, E = 1500 MPa, p = 0.1 MPa is shown), larger amounts of immature bone, cartilage and fibrous tissues are predicted to form (Fig. 8(c)) compared to an optimized configuration.

3.2. Effect of the length L of the beam elements included in the unit cell

Increasing values of L lead to increasing values of D (Figs. 9(a), 9(c), 9(d) and 9(f)), which is consistent with the physics of the problem. In fact, as L increases, the global scaffold stiffness decreases. Therefore, in order to re-establish the original scaffold stiffness, the algorithm increases the dimension D. However, changing the dimension L does not lead to significant changes of $BO_{\%MAX}$. In fact, the curves representing $BO_{\%MAX}$ in function of the load p are practically overlapped (Figs. 9(b) and 9(e)), which indicates that $BO_{\%MAX}$ is rather insensitive to the specific value fixed for L. Only the results referring to the case E = 1000 MPa are shown in the Figure 9. Diagrams obtained for the other hypothesized scaffold Young's moduli are similar to those shown in Figure 8 and therefore, for the sake of brevity, omitted. Interestingly, for variable values of L, $p_{saturation}$ remains constant (Figs. 9(a) and 9(d)), which means that the saturation load does not depend on the dimension L.

3.3. Comparison with other scaffold unit cells: performance maps

In order to determine, for different load levels, the best unit cell that allows maximizing the bone formation, the amounts of bone predicted for different geometries were compared. Depending

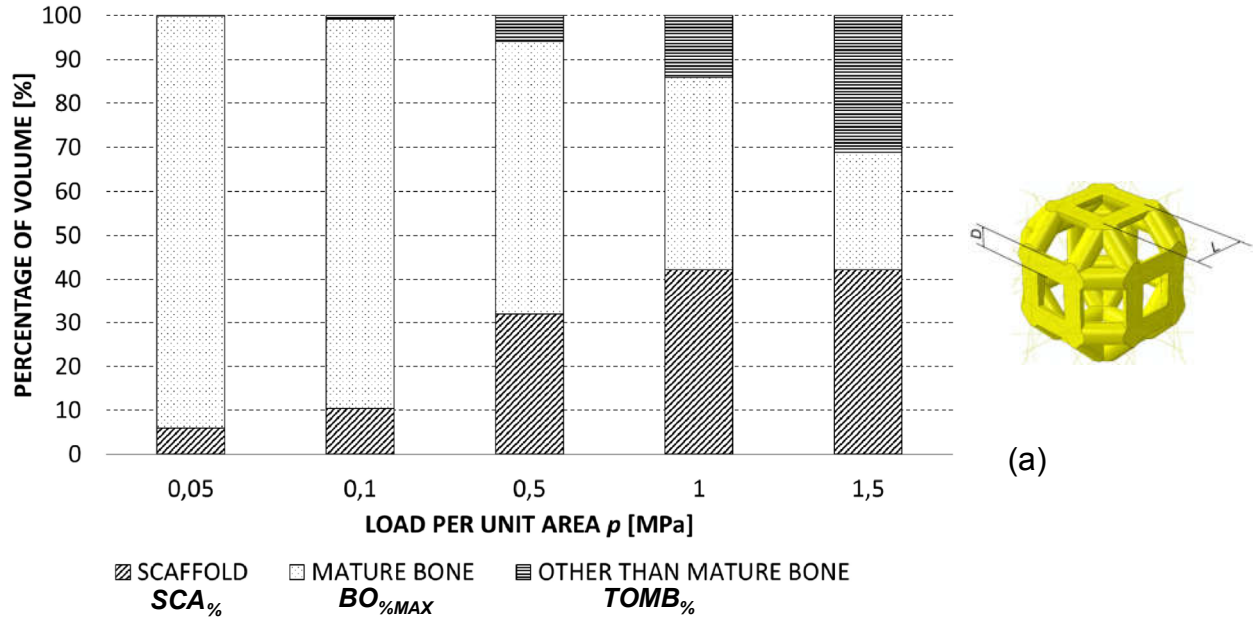

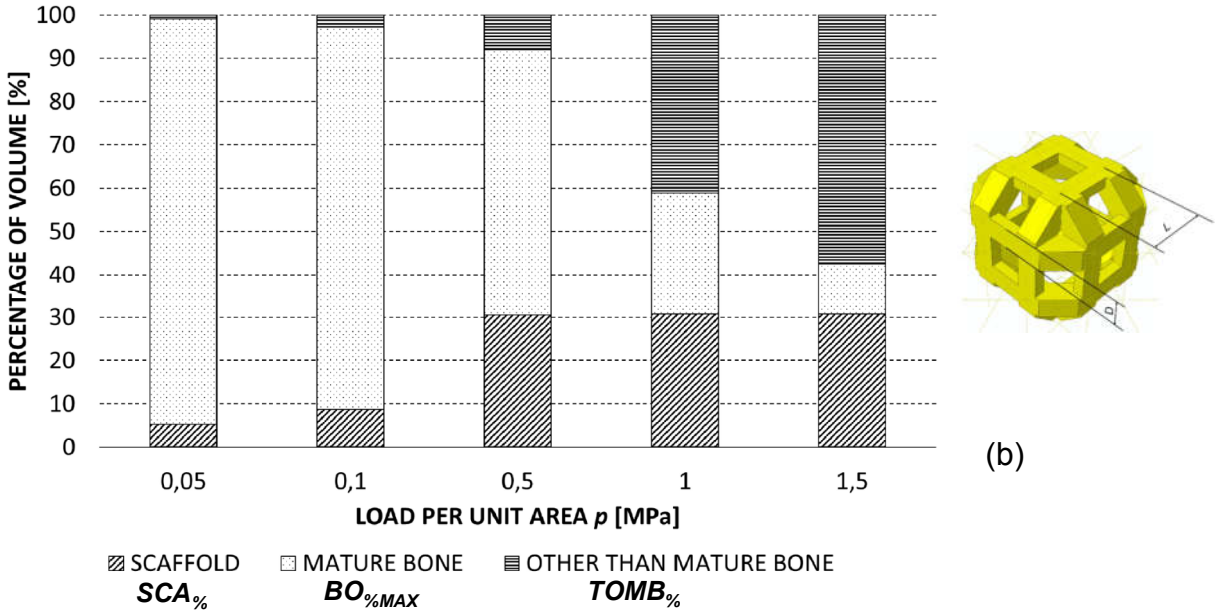

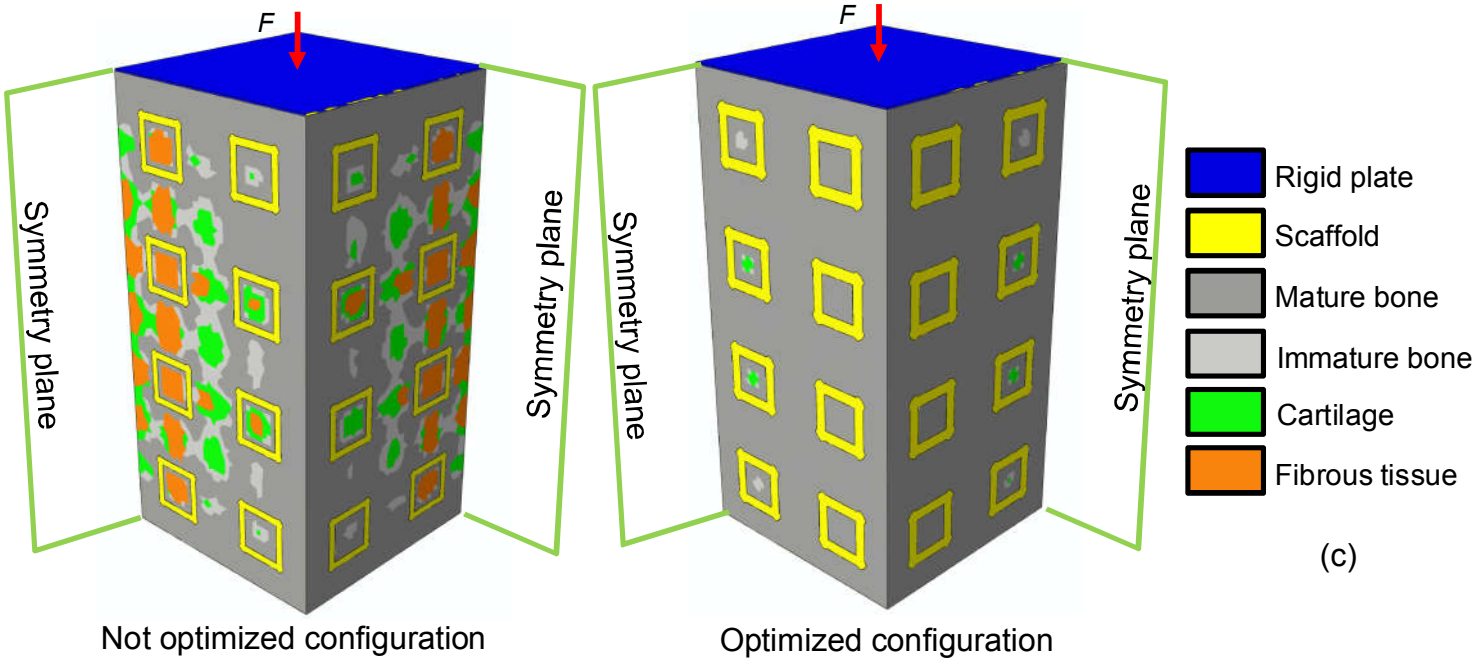

Fig. 8. Percentage of volume occupied by mature bone, scaffold and tissues other than mature bone predicted in both, circular (a) and square (b) section, E = 1000 MPa. The percentage of volume occupied by mature bone corresponds to $BO_{\%MAX}$. Patterns of the tissues differentiating within the scaffold pores (circular section, E = 1500 MPa, p = 0.1 MPa) in a not optimized (D = 40 μm) and optimized (D = 58 μm) scaffold configuration.

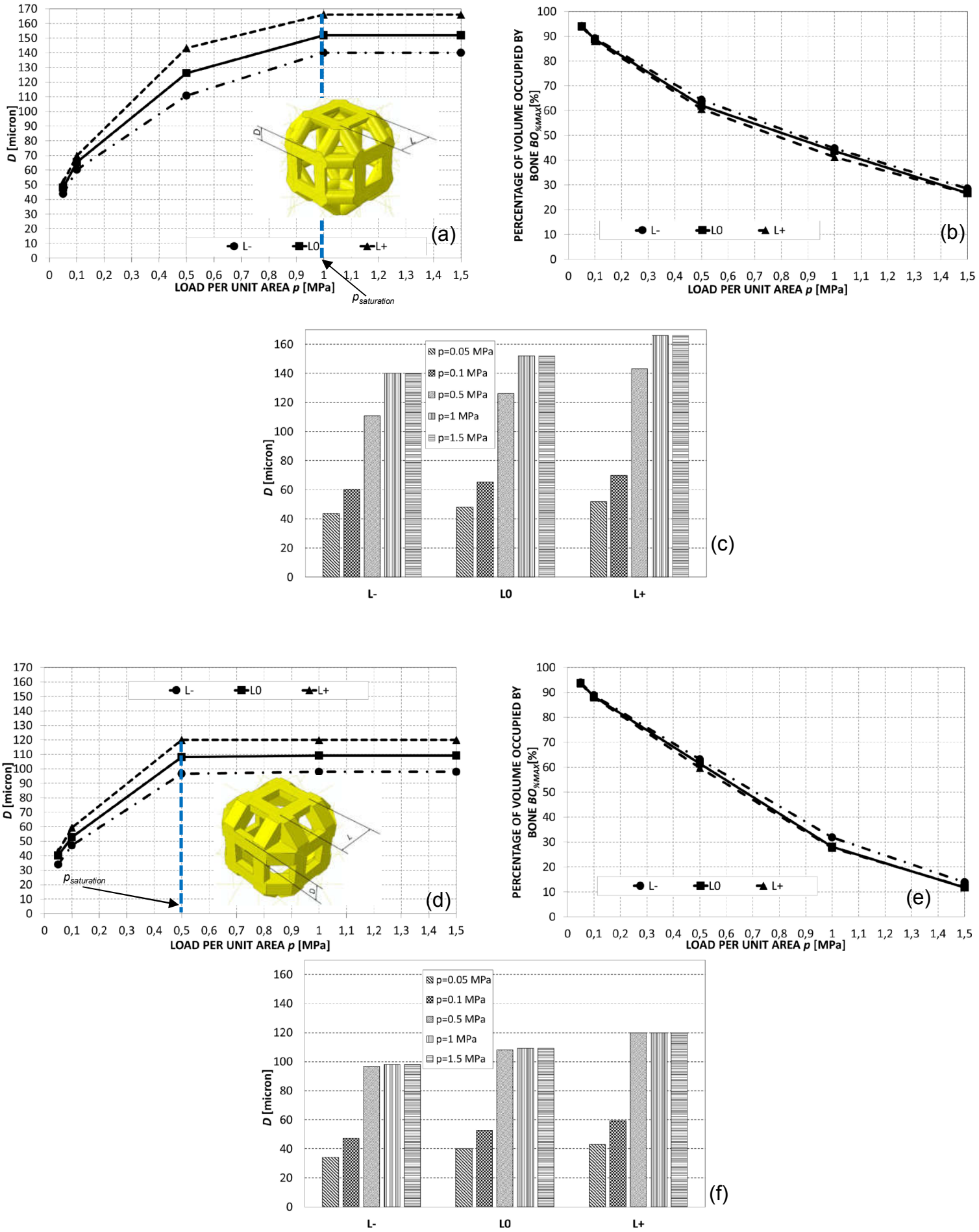

Fig. 9. Values of D (a, d) and $BO_{\%MAX}$ (b, e) predicted by the algorithm for different values of L in the case of circular (a, b) and square (d, e) cross-section. Values of D expressed in function of the dimension L for the circular (c) and square (f) cross-section. Increasing values of L lead to increasing values of D, which is consistent with the physics of the problem. In fact, as L increases, the global scaffold stiffness decreases. Therefore, in order to re-establish the original scaffold stiffness, the algorithm increases the dimension D. For the sake of brevity, only the results referring to E = 1000 MPa are shown in the figure.

on the compressive load acting on the scaffold, we evaluated if and when a given unit cell is preferable to others. In other words, we traced performance maps that allow to determine, for different values of the compressive load p, the best scaffold type/geometry (Fig. 10).

$BO_{\%MAX}$ values obtained for the circular cross-section were compared with those related to the square one (Fig. 10(a)). Different regions highlighted with different colours were identified. For low load values (< 0.5 MPa, i.e. region highlighted in yellow) using a circular cross-section is equivalent to using a square cross-section. For load levels higher than 0.5 MPa, instead (i.e. region highlighted in blue), the circular cross-section performs better than the square one, as for the circular cross-section larger amounts of bone are predicted to form. However, for all the hypothesized levels of load, the volume occupied by the scaffold $SCA_{\%}$ in the case of circular cross-section appears larger than the counterpart predicted for the square one (Fig. 10(b)). $BO_{\%MAX}$ values computed in this study were also compared with those obtained for simpler unit cells (Figs. 10(c) and 10(e)), namely, a hexahedron (or, more precisely, a rectangular cuboid) unit cell obtained by realizing in a cubic volume: (i) Elliptic (or Circular) Pores (EoCP) (Fig. 10(c)) or (ii) Rectangular (or Square) Pores (RoSP) (Fig. 10(e)). In detail, rhombicuboctahedron unit cell/ circular cross-section was compared with EoCP unit cell, while rhombicuboctahedron unit cell/square cross-section with RoSP unit cell. For all the hypothesized load values, RoSP unit cell performs better than the rhombicuboctahedron unit cell/square cross-section (Fig. 10(e), see region highlighted in red). In particular, the hexahedron unit cell with rectangular cross-section presents the smallest values of $SCA_{\%}$ (Fig. 10(f)). Interestingly, for all the hypothesized values of the compressive load p, the scaffold with hexahedron unit cell, rectangular pores, exhibits values of $SCA_{\%}$ smaller than those computed for hexahedron unit cell, square pores. This can be justified with the argument that in the case of rectangular pores, two design variables have to be optimized (i.e. the height and the width of the rectangle) and then greater $BO_{\%MAX}$ values, - or, equivalently, smaller values of $SCA_{\%}$ - can be obtained than the case where just one design variable (i.e. the lenght of the square side) can be optimized (Fig. 10(f)). For low load levels (<≈ 0.2 MPa, region highlighted in green) the rhombicuboctahedron unit cell/circular cross-section performs better

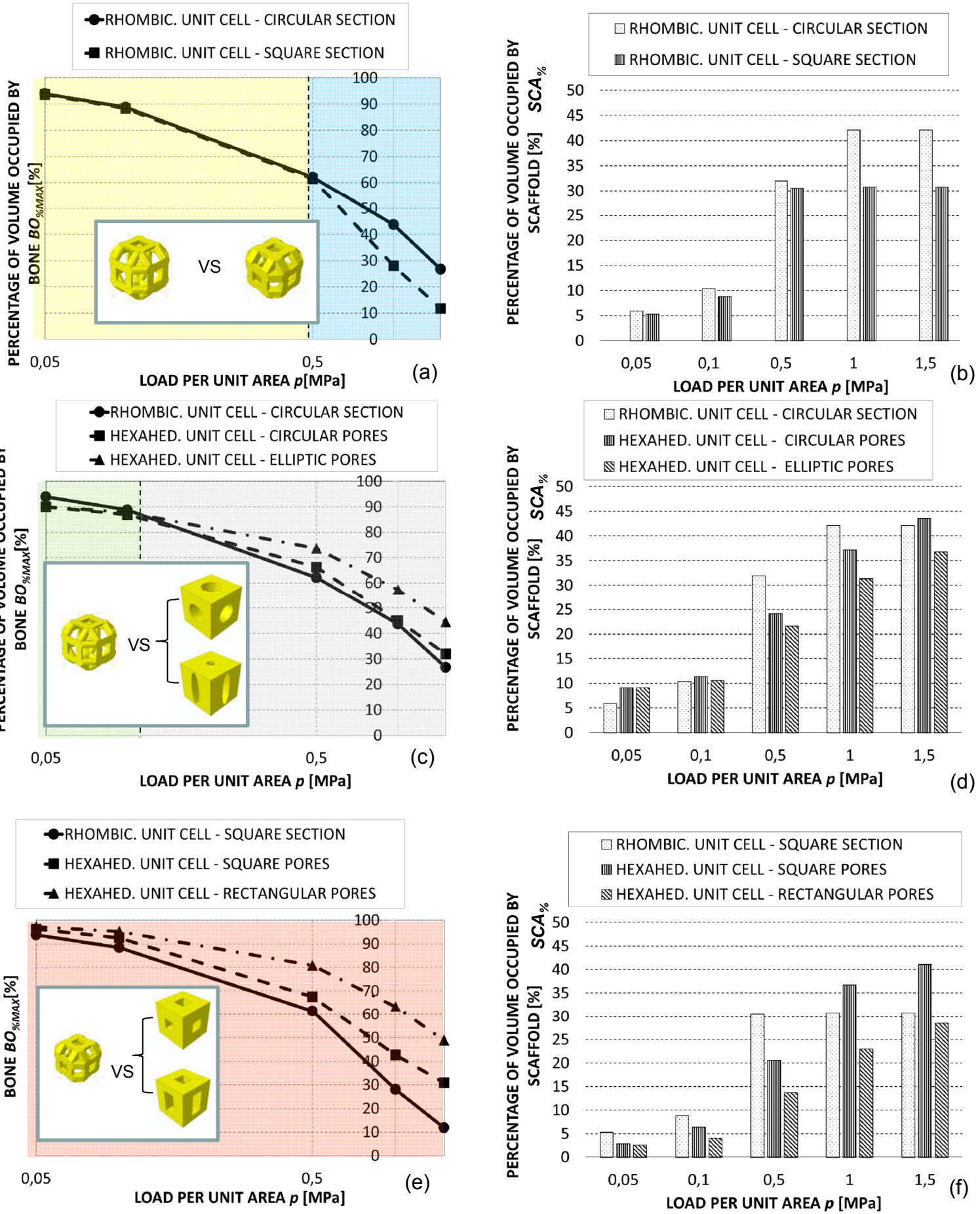

Fig. 10. Performance maps. Comparison between the percentage of bone predicted (a, c, e) and the percentage of volume occupied by scaffold (b, d, f) for different scaffold unit cells: (a-b) rhombicuboctahedron unit cell, circular cross-section vs. rhombicuboctahedron unit cell, square cross-section; (c-d) rhombicuboctahedron unit cell, circular cross-section vs. hexahedron unit cell with circular and elliptic pores (EoCP unit cell, data taken from Boccaccio *et al.* [30]); (e-f) rhombicuboctahedron unit cell, square cross-section vs. hexahedron unit cell with square and rectangular pores (RoSP unit cell, data taken from Boccaccio *et al.* [30]). In order to better visualize the results, a logarithmic scale was utilized on the axis of the load. Different regions highlighted with different colours were identified where a given unit cell geometry is preferable to others.

than the EoCP one; for higher loads, instead, the contrary occurs (Fig. 10(c), region highlighted in grey). Analogously, for low values of load, the volume $SCA_{\%}$ predicted for the rhombicuboctahedron unit cell/circular cross-section, appears to be smaller than that computed for EoCP. The contrary occurs for higher values of load (Fig. 10(d)) As observed above in the case of the RoSP unit cell, the volume $SCA_{\%}$ predicted for hexahedron unit cell, elliptic pores is always smaller than that computed for the hexahedron unit cell, circular pores (Fig. 10(d)). Again, this can be justified with the fact that for the elliptic pores two design variables (i.e. the major and the minor axes of the ellipse) has to be optimized while for the circular ones, just one (i.e. the radius of the circumference).

The proposed approach presents some limitations. First, a simplified model of the scaffold geometry was utilized. In general, scaffolds utilized in the orthopaedic surgery are much more complex structures with a large number of pores. Modelling such structures would require a computational cost tremendously high thus making its implementation into the clinical context *de facto* not affordable. However, predictions carried out with the proposed approach on small portions of the scaffold actually implanted can certainly be performed and give a reasonably good idea about the best scaffold geometry. Second, predictions of the optimal scaffold geometry were carried out based on the values of the biophysical stimulus S registered within the granulation tissue during the early stages of the bone development process. Ideally, the best scaffold geometry should be determined considering the values of S during the entire time window that goes from the scaffold implantation until the completion of the healing process. However, introducing the variable time in the optimization process would make the algorithm much, much more expensive in terms of the computational time and this, again, would make its implementation into the clinical context very critical. Strictly related to this, is the (third) limitation that in the study scaffold dissolution was not modelled. Ideally, for each scaffold geometry proposed by the algorithm as a possible candidate solution, the algorithm itself should simulate the dissolution process in time and based on the scaffold geometry after this time, the algorithm should re-propose new candidate solutions. On the basis of the experience of previous studies [41,50] where we simulated the healing process (in time) of bone

fractures, we can estimate that including and simulating the dissolution process would require a computational cost at least two orders of magnitude higher than that spent in the present study. Fourth, angiogenesis, which is another factor that can partially regulate the bone regeneration in scaffolds [51] was not included in the model. Increases in computational power will ultimately allow more realistic models to be developed and the variable time to be taken into account. Fifth, simplified boundary and loading conditions were hypothesized. For instance, a rigid plate was utilized to load the scaffold but, in reality, the scaffold will be presumably loaded by bone or other "biological materials" which possess specific poroelastic properties that were not taken into account in the study. Furthermore, the transport of nutrients and oxygen to the cells occupying the scaffold pores was not simulated [52]. Sixth, new fabrication techniques are recently developing that allow the production of scaffolds within which different types of cells can attach, proliferate and differentiate [53,54]. Analyses on these new types of scaffolds should be carried out in the future. Seventh, coherently with the mechano-regulation diagram defined as in Lacroix and Prendergast [49], the predicted values of octahedral shear strain were, for the regions 'occupied' by bone, within the interval [0.04 ÷ 3.75] %. These values are consistent with those measured in osteocytes and osteoblasts in femur samples from rats [21]. Interstitial fluid flow values smaller than 3 μm/s were predicted for the regions 'occupied' by bone while higher values of this velocity were predicted for the regions occupied by cartilage (< 9 μm/s) or fibrous tissue (> 9μm/s). These values are a little bit smaller than the fluid velocity measured within the lacunar/canalicular system of a mechanically loaded bone [18] as well as the average interstitial fluid velocities predicted in osteocyte models subjected to loading levels representative of vigorous physiological activity [20]. However, the boundary and loading conditions utilized in these studies [18,20] are very different with respect to those hypothesized in this article. Eighth, for the values of load p considered in this study, the parameter S always had to be reduced (Fig. 6(c) and 7(c)). For instance, for decreasing levels of the Young's modulus the global scaffold stiffness decreases too, which leads to high values of S. The algorithm, then, tends to counterbalance this, increasing the cross-section dimension D thus reducing the biophysical stimulus S. However, we

expect that for lower levels of p, the contrary occurs, i.e. S has to be increased to avoid that in some regions within the scaffold pores, the bone resorption process takes place. This behavior was observed, for example, for the hexahedron unit cell [39] where, for loads $p \leq 0.01$ MPa, in large portions of the granulation tissue, very small values of S were predicted. This led the optimizer to increase as much as possible the dimensions of the pores thus making the scaffold more compliant and, consequently, increasing the average value of the biophysical stimulus S. In the present study, values of pressure so small were not considered for the following twofold reasons. (i) Considering loads $p \leq 0.01$ MPa, the optimizer predicts rhombicuboctahedron unit cells with very thin beam elements, which require a very very fine mesh. Preliminary investigations showed that the meshing these very thin structures requires at least $10 \div 15 \times 10^6$ elements with computational times tremendously longer than those spent in this study. (Note. In the case of the hexahedron unit cell, the meshing process of scaffolds with pores with increasing dimensions did not require to change the element dimensions as, instead, occurs in the case of the rhombicuboctahedron unit cell). (ii) Values of load $p \leq 0.01$ MPa have scarce relevance from the practical point of view as they are more than three orders of magnitude smaller than the ultimate strength in compression of the spongy bone [42] and hence significantly smaller than any actual physiological load.

In spite of these limitations, we observe that the predictions of the proposed model are consistent (Fig. 10) with those of previous studies [39] that successfully predicted the best geometry of scaffolds with hexahedron unit cells. Predictions of the proposed model are also consistent with the solutions of the analytical model proposed by Hedayati *et al.* [31]. In detail, in order to compare the results of the proposed model with those of the Hedayati *et al.* one, the following steps were followed. The only scaffold model (granulation tissue excluded) was first generated (with the following values of $D = 60$, 80, 100 and 120 μm for the circular cross-section and $D = 60$, 80 and 100 μm for the square cross-section) and then subjected to a compression load $p = 0.1$ MPa (Fig. 11). The resulting displacement fields u_2 were predicted in both cases, circular and square cross-section (Fig. 11(b)). The usual definition of elastic modulus was then employed to determine the apparent Young's

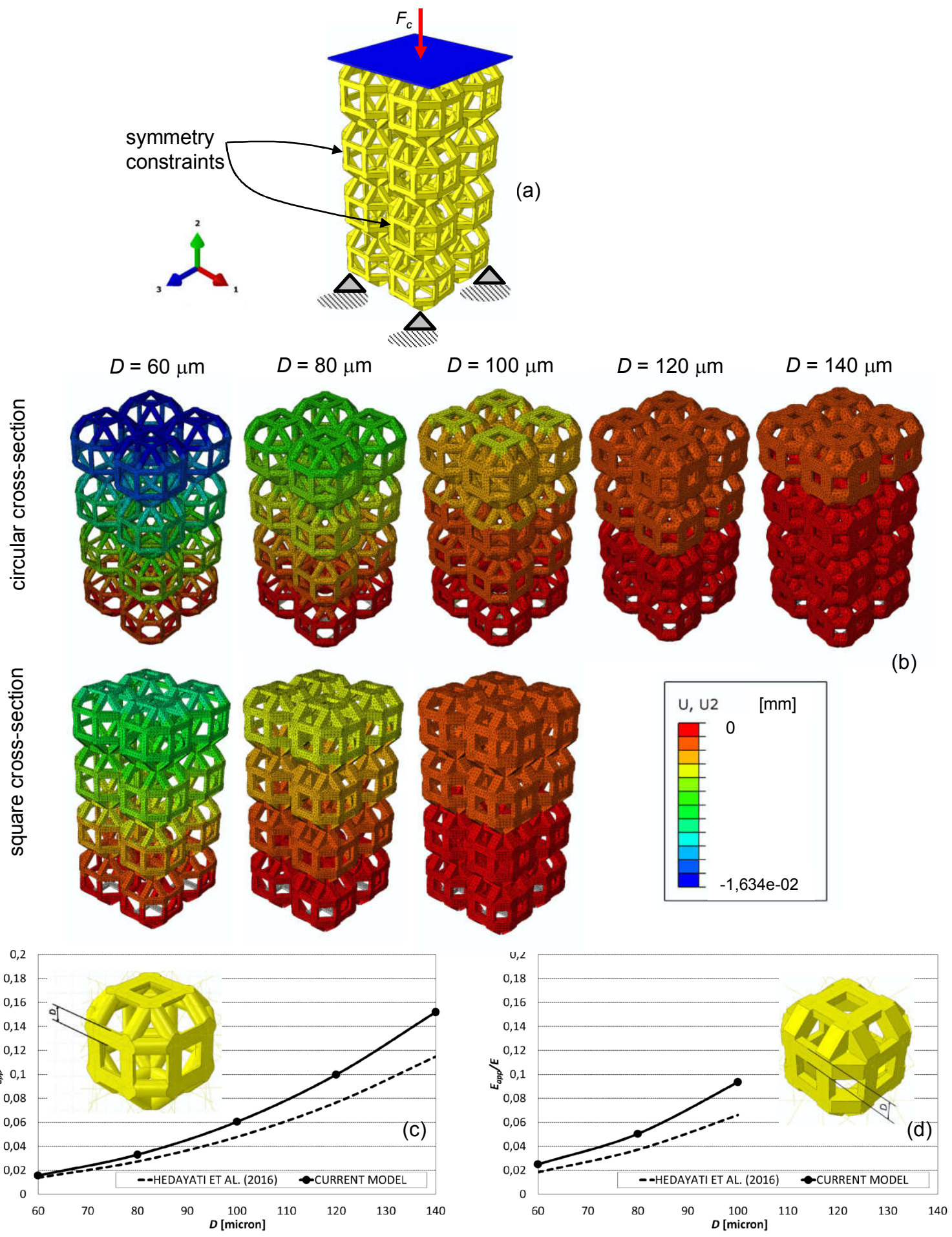

Fig. 11. Corroboration/validation of the proposed model. The scaffold model was subjected to a compression load p = 0.1 MPa (a). The resulting displacement fields u_2 were predicted for different values of D in both, circular and square cross-section (b). The usual definition of elastic modulus was employed to determine the apparent Young's modulus E_{app} for the scaffold structure. Based on the FE predictions, the ratio E_{app}/E was computed for different levels of D and compared with that obtained via the analytical solution by Hedayati *et al.* [22]. Comparison was carried out for both, circular (c) and square (d) cross-section.

modulus E_{app} for the scaffold structure. Specifically, if u_2 is the displacement along the direction 2 (Fig. 11(a)) of the rigid plate after the application of the load (per unit area) p, the apparent Young's modulus is given by: $E_{app} = p \cdot h / u_2$, being h the height of the scaffold model (Fig. 2). Based on the FE predictions, the ratio E_{app}/E was computed for different levels of D and compared with that obtained via the analytical solution by Hedayati *et al.* [31] that is briefly summarized in the Appendix. Interestingly, for small values of D, i.e. for the condition of slender beam, predictions of our model are close to those obtained via the analytical model. However, as we move towards the condition of large values of D, i.e. the condition of deep beam, the analytical solution starts to deviate, which is consistent with our expectations in consideration of the fact that the Euler-Bernoulli theory (on which the analytical solution is based), does not account for the effect of slenderness/depth of beams. It is worthy to note that the computed values of the ratio E_{app}/E are consistent with those of the trabecular bone tissue. Assuming an apparent Young's modulus for the spongy bone of $E_{app\_trab\_bone} = 580$ MPa (i.e. the average value of the experimental values measured by Odgaard and Linde [55]) and an elastic modulus of individual trabeculae of $E_{trabeculae} = 12600$ MPa (i.e. the average of the experimental values measured by Rho *et al.* [56]) the ratio $E_{app\_trab\_bone} / E_{trabeculae} = 0.046$ can be computed , which falls within the range of the values of E_{app}/E computed in this study (Figs. 11(c) and (d)).

The patterns of bony tissue predicted with the proposed model are also consistent with those observed in vivo in three dimensional matrix channels with different shapes [4]. In Figure 12 the experimental patterns of new tissue formed in square and triangular channels are compared to those predicted in square and triangular elements of the single rhombicuboctahedron unit cell. Specifically, grey elements shown in the figure are those for which the condition $n_{resorb} < S < n_{mature}$ is satisfied (i.e., formation of mature bone). Bone formation starts from the matrix wall and proceeds towards the centre while the sharp edges of the matrix are 'rounded' by the new formed tissue. This same behaviour was predicted by the proposed model (Figs. 12(a) and 12(b)).

The proposed algorithm well suits to the recent research lines more and more oriented towards customized medical solutions. Based on the antropometric data of the specific patient and on the

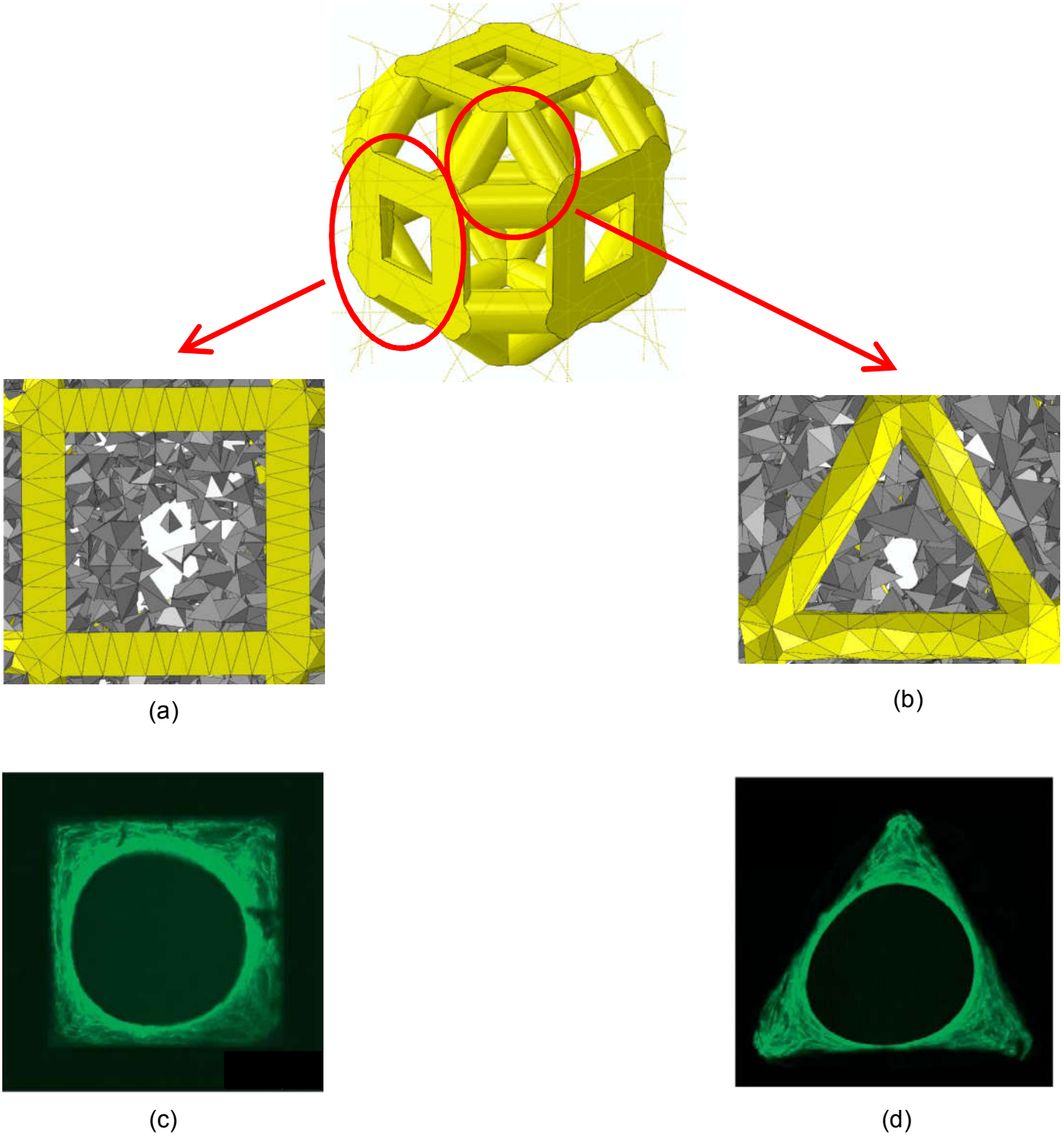

Fig. 12. Corroboration/validation of the proposed model. Patterns of bony tissue predicted to form within square (a) and triangular (b) elements of the rhombicuboctahedron unit cell compared with patterns of new tissue formed in three-dimensional matrix channels with square (c) and triangular (d) shape (Figures (c) and (d) have been taken from Rumpler *et al.* [4]).

morphology of the specific anatomic region - where scaffold must be implanted -, the possible boundary and loading conditions acting on the scaffold itself can be hypothesized. Therefore, utilizing the proposed algorithm, one could determine the optimal geometry design that encourages bone growth thus maximizing the bone formation. The performance maps (Fig. 10) traced with the proposed algorithm, can guide the orthopaedic/surgeon in the choice of the best scaffold to be implanted into a patient-specific anatomic region.

4. Conclusions

A mechanobiology-based optimization algorithm was developed to determine the best geometry of scaffolds for bone tissue engineering made from rhombicuboctahedron unit cells. In spite of the huge number of articles on regular porous biomaterials made from different unit cells, mechanobiology of tissue differentiation in such scaffolds remains unclear. We proposed the first study ever reported in the literature where the best geometry of scaffolds with rhombicuboctahedron unit cell was determined via a mechanobiology-based optimization algorithm.

For different cross-section shapes and for different values of the: (i) scaffold Young's modulus, (ii) length of the beam elements included in the unit cell and (iii) compressive load acting on the scaffold upper surface, the optimal cross-section dimension D was determined.

The algorithm predicts that the circular cross-section performs better than the square one. The scaffold performances appear rather insensitive to the length of the beam elements included in the unit cell.

We compared the performances of the proposed scaffold type with those of other scaffolds based on simple hexahedron unit cells. In detail, the amounts of bone and the solid volume fraction were compared. We also identified different load levels where the use of a given unit cell is preferable to others and vice-versa. We found that for high compressive loads, scaffolds with hexahedron unit cell perform better than those utilizing the rhombicuboctahedron one. For low load values, instead,

rhombicuboctahedron unit cell exhibits performances comparable and even better than those of hexahedron unit cell.

The bony patterns predicted with the proposed model appear reasonably consistent with those observed in *in vitro* studies.

In a context that becomes more and more oriented towards customized solutions the proposed algorithm appears a promising tool. Based on the anthropometric data of the specific patient as well as on the specific anatomy of the region where the scaffold must be implanted, one can hypothesize the possible values of the load acting on the scaffold structure and, implementing the proposed model, 'identify' the best scaffold that is better suited to the specific scope. The performance maps traced with the proposed algorithm, can guide the orthopaedic/surgeon in the choice of the best scaffold to be implanted into a patient-specific anatomic region.

Appendix

Based on the Euler-Bernoulli beam theory, Hedayati *et al.* [31] related for both, the circular and the square cross-section, the apparent Young's modulus E_{app} with the scaffold Young's modulus E through the quantities D, L_0 and the apparent Poisson's ratio v_{app}. The analytical solution for circular cross-section with radius $r = D/2$ is given by the following system of equations:

$$\begin{cases} \dfrac{E_{app}}{E} = \dfrac{4\pi\left(\frac{r}{L_0}\right)^2}{3\left(1+\sqrt{2}\right)}\left[\dfrac{4+108\left(\frac{r}{L_0}\right)^2+207\left(\frac{r}{L_0}\right)^4+81\left(\frac{r}{L_0}\right)^6+\frac{1}{2\left(1+v_{app}\right)}\left(\frac{2}{3}+19\left(\frac{r}{L_0}\right)^2+45\left(\frac{r}{L_0}\right)^4+18\left(\frac{r}{L_0}\right)^6\right)}{8+70\left(\frac{r}{L_0}\right)^2+105\left(\frac{r}{L_0}\right)^4+27\left(\frac{r}{L_0}\right)^6+\frac{1}{2\left(1+v_{app}\right)}\left(\frac{4}{3}+13\left(\frac{r}{L_0}\right)^2+23\left(\frac{r}{L_0}\right)^4+6\left(\frac{r}{L_0}\right)^6\right)}\right] \\ r = \dfrac{D}{2} \\ v_{app} = \dfrac{1}{3}\dfrac{8-12\left(\frac{r}{L_0}\right)^2-36\left(\frac{r}{L_0}\right)^4+\frac{1}{2\left(1+v_{app}\right)}\left(\frac{4}{3}-\left(\frac{r}{L_0}\right)^2-\left(\frac{r}{L_0}\right)^4\right)}{8+70\left(\frac{r}{L_0}\right)^2+105\left(\frac{r}{L_0}\right)^4+27\left(\frac{r}{L_0}\right)^6+\frac{1}{2\left(1+v_{app}\right)}\left(\frac{4}{3}+13\left(\frac{r}{L_0}\right)^2+23\left(\frac{r}{L_0}\right)^4+6\left(\frac{r}{L_0}\right)^6\right)} \end{cases} \quad Eq.(A.1)$$

Analogously, the analytical solution for square cross-section with side long D is given by:

$$\begin{cases} \dfrac{E_{app}}{E} = \dfrac{4\left(\frac{D}{L_0}\right)^2}{\left(1+\sqrt{2}\right)}\left[\dfrac{12+108\left(\frac{D}{L_0}\right)^2+69\left(\frac{D}{L_0}\right)^4+9\left(\frac{D}{L_0}\right)^6+\frac{1}{2(1+\upsilon_{app})}\left(2+19\left(\frac{D}{L_0}\right)^2+15\left(\frac{D}{L_0}\right)^4+2\left(\frac{D}{L_0}\right)^6\right)}{72+210\left(\frac{D}{L_0}\right)^2+105\left(\frac{D}{L_0}\right)^4+9\left(\frac{D}{L_0}\right)^6+\frac{1}{2(1+\upsilon_{app})}\left(12+39\left(\frac{D}{L_0}\right)^2+23\left(\frac{D}{L_0}\right)^4+2\left(\frac{D}{L_0}\right)^6\right)}\right] \\ \upsilon_{app} = \dfrac{24-12\left(\frac{D}{L_0}\right)^2-12\left(\frac{D}{L_0}\right)^4+\frac{1}{2(1+\upsilon_{app})}\left(4-\left(\frac{D}{L_0}\right)^2-3\left(\frac{D}{L_0}\right)^4\right)}{72+210\left(\frac{D}{L_0}\right)^2+105\left(\frac{D}{L_0}\right)^4+9\left(\frac{D}{L_0}\right)^6+\frac{1}{2(1+\upsilon_{app})}\left(12+39\left(\frac{D}{L_0}\right)^2+23\left(\frac{D}{L_0}\right)^4+2\left(\frac{D}{L_0}\right)^6\right)} \end{cases} \quad Eq.(A.2)$$

References

1. P. Bianco, P.G. Robey, Stem cells in tissue engineering. Nature 414 (2001) 118–121.
2. S.J. Hollister, Porous scaffold design for tissue engineering. Nat. Mater. 4 (2005) 518–524.
3. A.A. Zadpoor, Bone tissue regeneration: the role of scaffold geometry. Biomater. Sci. 3 (2015) 231–245.
4. M. Rumpler, A. Woesz, J.W. Dunlop, J.T. van Dongen, P. Fratzl, The effect of geometry on three-dimensional tissue growth. J. R. Soc. Interface 5 (2008) 1173–1180.
5. D.P. Byrne, D. Lacroix, J.A. Planell, D.J. Kelly, P.J. Prendergast, Simulation of tissue differentiation in a scaffold as a function of porosity, Young's modulus and dissolution rate: application of mechanobiological models in tissue engineering. Biomaterials 28 (2007) 5544–5554.
6. J.L. Milan, J.A. Planell, D. Lacroix, Simulation of bone tissue formation within a porous scaffold under dynamic compression. Biomech. Model. Mechanobiol. 9 (2010) 583–596.
7. W.J. Hendrikson, C.A. van Blitterswijk, N. Verdonschot, L. Moroni, J. Rouwkema, Modeling Mechanical Signals on the Surface of μCT and CAD Based Rapid Prototype Scaffold Models to Predict (Early Stage) Tissue Development. Biotechnol. Bioeng. 111 (2014) 1864–1875.
8. A. Boccaccio, A. Ballini, C. Pappalettere, D. Tullo, S. Cantore, A. Desiate, Finite Element Method (FEM), Mechanobiology and Biomimetic Scaffolds in Bone Tissue Engineering. Int. J. Biol. Sci. 7 (2011) 112–132.
9. M.A. Velasco, C.A. Narváez-Tovar, D.A. Garzón-Alvarado, Design, Materials, and Mechanobiology of Biodegradable Scaffolds for Bone Tissue Engineering. Biomed Res. Int. Article ID 729076 (2015) 21 pages.
10. A. O'Reilly, D.J. Kelly, A Computational Model of Osteochondral Defect Repair Following Implantation of Stem Cell-Laden Multiphase Scaffolds. Tissue Eng. Part A. 23 (2017) 30–42.

11. A. Entezari, S.I. Roohani-Esfahani, Z. Zhang, H. Zreiqat, C.R. Dunstan, Q. Li, Fracture behaviors of ceramic tissue scaffolds for load bearing applications. Sci. Rep. 6 (2016) Art. no: 28816.

12. M.C.H. van der Meulen, R. Huiskes, Why mechanobiology? A survey article. J. Biomech. 35 (2002) 401–414.

13. C. Jungreuthmayer, M.J. Jaasma, A.A. Al-Munajjed, J. Zanghellini, D.J. Kelly, F.J. O'Brien, Deformation simulation of cells seeded on a collagen-GAG scaffold in a flow perfusion bioreactor using a sequential 3D CFD-elastostatics model. Med. Eng. Phys. 31 (2009) 420–427.

14. R.J. McCoy, C. Jungreuthmayer, F.J. O'Brien, Influence of flow rate and scaffold pore size on cell behavior during mechanical stimulation in a flow perfusion bioreactor. Biotechnol. Bioeng. 109 (2012) 1583–1594.

15. F. Zhao, T.J. Vaughan, L.M. McNamara, Multiscale fluid–structure interaction modelling to determine the mechanical stimulation of bone cells in a tissue engineered scaffold. Biomech. Model. Mechanobiol. 14 (2015) 231–243.

16. F. Zhao, T.J. Vaughan, L.M. McNamara, Quantification of fluid shear stress in bone tissue engineering scaffolds with spherical and cubical pore architectures. Biomech. Model. Mechanobiol. 15 (2016) 561–577.

17. E. Anderson, M.L. Knothe Tate, Idealization of pericellular fluid space geometry and dimension results in a profound underprediction of nano-microscale stresses imparted by fluid drag on osteocytes. J. Biomech. 41 (2008) 1736–1746.

18. C. Price, X. Zhou, W. Li, L. Wang, Real-time measurement of solute transport within the lacunar-canalicular system of mechanically loaded bone: Direct evidence for load-induced fluid flow. J. Bone Miner. Res. 26 (2011) 277–285.

19. S.W. Verbruggen, T.J. Vaughan, L.M. McNamara, Strain amplification in bone mechanobiology: a computational investigation of the in vivo mechanics of osteocytes. J. R. Soc. Interface 9 (2012) 2735–2744.
20. S.W. Verbruggen, T.J. Vaughan, L.M. McNamara, Fluid flow in the osteocyte mechanical environment: a fluid–structure interaction approach. Biomech. Model. Mechanobiol. 13 (2014) 85–97.
21. S.W. Verbruggen, M.J. Mc Garrigle, M.G. Haugh, M.C. Voisin, L.M. McNamara, Altered Mechanical Environment of Bone Cells in an Animal Model of Short- and Long-Term Osteoporosis. Biophys. J. 108 (2015) 1587–1598.
22. Y. Jiang, Q. Wang, Highly-stretchable 3D-architected Mechanical Metamaterials. Sci. Rep. 6 (2016) Art. no. 34147.
23. G. Campoli, M.S. Borleffs, S. Amin Yavari, R. Wauthle, H. Weinans, A.A. Zadpoor, Mechanical properties of open-cell metallic biomaterials manufactured using additive manufacturing. Mater. Design 49 (2013) 957–965.
24. J. Parthasarathy, B. Starly, S. Raman, A. Christensen, Mechanical evaluation of porous titanium (Ti6Al4V) structures with electron beam melting (EBM). J. Mech. Behav. Biomed. Mater. 3 (2010) 249–259.
25. S.A. Yavari, R. Wauthle, J. van der Stok, A.C. Riemslag, M. Janssen, M. Mulier, J.P. Kruth, J. Schrooten, H. Weinans, A.A. Zadpoor, Fatigue behavior of porous biomaterials manufactured using selective laser melting. Mater. Sci. Eng. C 33 (2013) 4849–4858.
26. X. Zheng, H. Lee, T.H. Weisgraber, M. Shusteff, J. DeOtte, E.B. Duoss, J.D. Kuntz, M.M. Biener, Q. Ge, J.A. Jackson, S.O. Kucheyev, N.X. Fang, C.M. Spadaccini, Ultralight, ultrastiff mechanical metamaterials. Science 344 (2014) 1373–1377.
27. B. Buffel, F. Desplentere, K. Bracke, I. Verpoest, Modelling open cell-foams based on the Weaire–Phelan unit cell with a minimal surface energy approach. Int. J. Solids Struct. 51 (2014) 3461–3470.

28. E. Ptochos, G. Labeas, Shear Modulus Determination of Cuboid Metallic Open-Lattice Cellular Structures by Analytical, Numerical and Homogenisation Methods. Strain 48 (2012) 415–429.

29. E. Ptochos, G. Labeas, Elastic modulus and Poisson's ratio determination of micro-lattice cellular structures by analytical, numerical and homogenisation methods. J. Sandw. Struct. Mater. 14 (2012) 597–626.

30. S.M. Ahmadi, G. Campoli, S. Amin Yavari, B. Sajadi, R. Wauthle, J. Schrooten, H. Weinans, A.A. Zadpoor, Mechanical behavior of regular open-cell porous biomaterials made of diamond lattice unit cells. J. Mech. Behav. Biomed. Mater. 34 (2014) 106–115.

31. R. Hedayati, M. Sadighi, M. Mohammadi-Aghdam, A.A. Zadpoor, Mechanics of additively manufactured porous biomaterials based on the rhombicuboctahedron unit cell. J. Mech. Behav. Biomed. Mater. 53 (2016) 272–294.

32. R. Hedayati, M. Sadighi, M. Mohammadi-Aghdam, A.A. Zadpoor, Mechanical properties of regular porous biomaterials made from truncated cube repeating unit cells: Analytical solutions and computational models. Mater. Sci. Eng. C 60 (2016) 163–183.

33. S.M. Giannitelli, D. Accoto, M. Trombetta, A. Rainer, Current trends in the design of scaffolds for computer-aided tissue engineering. Acta Biomater. 10 (2014) 580–594.

34. A. Rainer, S.M. Giannitelli, D. Accoto, S. De Porcellinis, E. Guglielmelli, M. Trombetta, Load-Adaptive Scaffold Architecturing: A Bioinspired Approach to the Design of Porous Additively Manufactured Scaffolds with Optimized Mechanical Properties. Ann. Biomed. Eng. 40 (2012) 966–975.

35. M.R. Dias, J.M. Guedes, C.L. Flanagan, S.J. Hollister, P.R. Fernandes, Optimization of scaffold design for bone tissue engineering: A computational and experimental study. Med. Eng. Phys. 36 (2014) 448–457.

36. P.G. Coelho, S.J. Hollister, C.L. Flanagan, P.R. Fernandes, Bioresorbable scaffolds for bone tissue engineering: optimal design, fabrication, mechanical testing and scale-size effects analysis. Med. Eng. Phys. 37 (2015) 287–296.

37. Y. Guyot, I. Papantoniou, Y.C. Chai, S. Van Bael, J. Schrooten, L. Geris, A computational model for cell/ECM growth on 3D surfaces using the level set method: a bone tissue engineering case study. Biomech. Model. Mechanobiol. 13 (2014) 1361–1371.

38. J. Wieding, A. Wolf, R. Bader, Numerical optimization of open-porous bone scaffold structures to match the elastic properties of human cortical bone. J. Mech. Behav. Biomed. Mater. 37 (2014) 56–68.

39. A. Boccaccio, A.E. Uva, M. Fiorentino, L. Lamberti, G. Monno, A Mechanobiology-based Algorithm to Optimize the Microstructure Geometry of Bone Tissue Scaffolds. Int. J. Biol. Sci. 12 (2016) 1–17.

40. A. Boccaccio, A.E. Uva, M. Fiorentino, G. Mori, G. Monno, Geometry Design Optimization of Functionally Graded Scaffolds for Bone Tissue Engineering: A Mechanobiological Approach. PLoS ONE 11 (2016) Art. no. e0146935.

41. A. Boccaccio, D.J. Kelly, C. Pappalettere, A Mechano-Regulation Model of Fracture Repair in Vertebral Bodies. J. Orthop. Res. 29 (2011) 433–443.

42. T.M. Keaveny, W.C. Hayes, Mechanical properties of cortical and trabecular bone. Bone 7 (1993) 285–344.

43. S. Eshraghi, S. Das, Mechanical and microstructural properties of polycaprolactone scaffolds with one-dimensional, two-dimensional, and three-dimensional orthogonally oriented porous architectures produced by selective laser sintering. Acta Biomater. 6 (2010) 2467–2476.

44. A. Boccaccio, C. Pappalettere, D.J. Kelly, The influence of expansion rates on mandibular distraction osteogenesis: a computational analysis. Ann. Biomed. Eng. 35 (2007) 1940–1960.

45. A. Boccaccio, P.J. Prendergast, C. Pappalettere, D.J. Kelly, Tissue differentiation and bone regeneration in an osteotomized mandible: a computational analysis of the latency period. Med. Biol. Eng. Comput. 46 (2008) 283–298.

46. A. Boccaccio, L. Lamberti, C. Pappalettere, Effects of aging on the latency period in mandibular distraction osteogenesis: a computational mechano-biological analysis. J. Mech. Med. Biol. 8 (2009) 203–225.

47. P.J. Prendergast, R. Huiskes, K. Søballe, Biophisical stimuli on cells during tissue differentiation at implant interfaces. J. Biomech. 30 (1997) 539–548.

48. R. Huiskes, W.D. van Driel, P.J. Prendergast, K. Søballe, A biomechanical regulatory model of periprosthetic tissue differentiation. J. Mater. Sci. Mater. Med. 8 (1997) 785–788.

49. D. Lacroix, P.J. Prendergast, A mechano-regulation model for tissue differentiation during fracture healing: analysis of gap size and loading. J. Biomech. 35 (2002) 1163–1171.

50. A. Boccaccio, D.J. Kelly, C. Pappalettere, A model of tissue differentiation and bone remodelling in fractured vertebrae treated with minimally invasive percutaneous fixation. Med. Biol. Eng. Comput. 50 (2012) 947–959.

51. C. Sandino, S. Checa, P.J. Prendergast, D. Lacroix, Simulation of angiogenesis and cell differentiation in a CaP scaffold subjected to compressive strains using a lattice modeling approach. Biomaterials 31 (2010) 2446–2452.

52. B.L. Jr. Vaughan, P.A. Galie, J.P. Stegemann, J.B. Grotberg, A poroelastic model describing nutrient transport and cell stresses within a cyclically strained collagen hydrogel. Biophys. J. 105 (2013) 2188–2198.

53. I.M. El-Sherbiny, M.H. Yacoub, Hydrogel scaffolds for tissue engineering: Progress and challenges. Glob. Cardiol. Sci. Pract. 2013 (2013) 316-342.

54. P.X. Ma, Biomimetic materials for tissue engineering. Adv. Drug Deliv. Rev. 60 (2008) 184–198.

55. A. Odgaard, F. Linde, The underestimation of Young's modulus in compressive testing of cancellous bone specimens. J. Biomech. 24 (1991) 691–698.

56. J.Y. Rho., R.B. Ashman, C.H. Turner, Young's modulus of trabecular and cortical bone material: Ultrasonic and microtensile measurements. J. Biomech. 26 (1993) 111–119.

Figure legends

Fig. 1. The generation of the rhombicuboctahedron unit cell was performed in seven subsequent steps (a-g). In the first step (a), an octagonal trajectory t_{oct} was traced, a circular or square cross-section was created and then, through the tool 'sweep' available in ABAQUS, a solid with the fixed cross-section was protruded along t_{oct}. All the sides of the octagonal trajectory t_{oct} were hypothesized to be equal and long L. The same procedure described in the first step (a) was successively repeated in the steps 2 to 5 ((b) to (f)) by adding a solid volume (protruded along t_{oct}) in each step. In the step 7 (g) the solid so obtained was cut along planes π_{Mi} (i=1, 2, …6) delimiting the cubic volume ($Q \times Q \times Q$, $Q = L \times (1 + 2 \cos(\pi/4))$ containing the unit cell. Rhombicuboctahedron unit cells with circular (h) and square (m) cross-section investigated in the study with indicated the dimensions L and D parameterized in the study. Three different values of L were hypothesized: $L = L_0 = 263{,}85$ μm, $L = L_- = L_0 \times 0{,}9$ and $L = L_+ = L_0 \times 1{,}1$. The entire scaffold geometry was obtained by successively mirroring the unit cell with respect to π_{Mi} planes.

Fig. 2. Boundary and loading conditions acting on the scaffold model. CAD model of the scaffold (a), granulation tissue (b) and entire (including 64 unit cells) system (scaffold + granulation tissue) (c). Exploiting the symmetry of the problem, a simplified model reproducing only 1/4 of the entire geometry was considered (d). (e) Detailed views of the simplified model with indicated the boundary and loading conditions acting on it. As the surrounding tissue would not totally prevent the fluid from escaping, the pore pressure p_{gr_tis} on the outer surfaces of the granulation tissue was set equal to zero to simulate the free exudation of fluid. On the symmetry planes instead, being null the fluid flow, the pore pressure must be $p_{sym} = \infty$.

Fig. 3. CAD model of the scaffold (a, f) and of the granulation tissue (b, g) in the case of circular (a, b) and square (f, g) cross-section. Finite element mesh of the scaffold (c, h), the granulation tissue (d,

m) and of the entire system (e, n) in the case of circular (c, d, e) and square (h, m, n) cross-section. The entire model (scaffold + granulation tissue) included about 5×10^6 elements with about 1×10^6 nodes.

Fig. 4. Schematic of the algorithm written in Matlab environment to determine the optimal dimension D for different values of load, Young's modulus and L and for different cross-section shapes.

Fig. 5. (a) Upper and lower bounds set for the dimension D for different cross-section shapes and values of L. Geometric configuration of the model for $D = D_{min}$ (b) and $D = D_{max}$ in the case of circular (c) and square (d) cross-section. Values of $D > D_{max}$ lead to close the aperture between the inclined sides (see detailed images (c) and (d)) thus changing the originally hypothesized connectivity scaffold.

Fig. 6. Optimization of the rhombicuboctahedron unit cell, circular cross-section. (a) Optimal scaffold geometries predicted by the algorithm, in the case of circular cross-section. Values of the optimal diameter D (b) and of $BO_{\%MAX}$ (c) predicted by the algorithm for different levels of load and scaffold Young's modulus. For the sake of clarity, the only saturation load $p_{saturation}$ related to E = 500 MPa is shown in the figure.

Fig. 7. Optimization of the rhombicuboctahedron unit cell, square cross-section. (a) Optimal scaffold geometries predicted by the algorithm, in the case of square cross-section. Values of the optimal diameter D (b) and of $BO_{\%MAX}$ (c) predicted by the algorithm for different levels of load and scaffold Young's modulus. For the sake of clarity, the only saturation load $p_{saturation}$ related to E = 500 MPa is shown in the figure.

Fig. 8. Percentage of volume occupied by mature bone, scaffold and tissues other than mature bone predicted in both, circular (a) and square (b) section, E = 1000 MPa. The percentage of volume occupied by mature bone corresponds to $BO_{\%MAX}$. Patterns of the tissues differentiating within the scaffold pores (circular section, E = 1500 MPa, p = 0.1 MPa) in a not optimized (D = 40 μm) and optimized (D = 58 μm) scaffold configuration.

Fig. 9. Values of D (a, d) and $BO_{\%MAX}$ (b, e) predicted by the algorithm for different values of L in the case of circular (a, b) and square (d, e) cross-section. Values of D expressed in function of the dimension L for the circular (c) and square (f) cross-section. Increasing values of L lead to increasing values of D, which is consistent with the physics of the problem. In fact, as L increases, the global scaffold stiffness decreases. Therefore, in order to re-establish the original scaffold stiffness, the algorithm increases the dimension D. For the sake of brevity, only the results referring to E = 1000 MPa are shown in the figure.

Fig. 10. Performance maps. Comparison between the percentage of bone predicted (a, c, e) and the percentage of volume occupied by scaffold (b, d, f) for different scaffold unit cells: (a-b) rhombicuboctahedron unit cell, circular cross-section vs. rhombicuboctahedron unit cell, square cross-section; (c-d) rhombicuboctahedron unit cell, circular cross-section vs. hexahedron unit cell with circular and elliptic pores (EoCP unit cell, data taken from Boccaccio *et al.* [39]); (e-f) rhombicuboctahedron unit cell, square cross-section vs. hexahedron unit cell with square and rectangular pores (RoSP unit cell, data taken from Boccaccio *et al.* [39]). In order to better visualize the results, a logarithmic scale was utilized on the axis of the load. Different regions highlighted with different colours were identified where a given unit cell geometry is preferable to others.

Fig. 11. Corroboration/validation of the proposed model. The scaffold model was subjected to a compression load p = 0.1 MPa (a). The resulting displacement fields u_2 were predicted for different

values of D in both, circular and square cross-section (b). The usual definition of elastic modulus was employed to determine the apparent Young's modulus E_{app} for the scaffold structure. Based on the FE predictions, the ratio E_{app}/E was computed for different levels of D and compared with that obtained via the analytical solution by Hedayati *et al.* [31]. Comparison was carried out for both, circular (c) and square (d) cross-section.

Fig. 12. Corroboration/validation of the proposed model. Patterns of bony tissue predicted to form within square (a) and triangular (b) elements of the rhombicuboctahedron unit cell compared with patterns of new tissue formed in three-dimensional matrix channels with square (c) and triangular (d) shape (Figures (c) and (d) have been taken from Rumpler *et al*. [4]).